Final Technical Report Instructions

Purpose: Provide DOE with a concise technical review on the final outcomes of an award including: technical impact, scholarship, and intellectual property. There should be sufficient detail to assess the project's results relative to the objectives, milestones, and go/no-go decision points. The final report should articulate the accomplishments made during the award and the importance of the results. The report must be a self-supporting document: from reading the report alone, the value of the work completed shall be apparent. The report demonstrates how the funded efforts have mitigated the technical risks and uncertainties associated with converging on the final deliverables.

Format: This report template is modeled after a technical manuscript for a peer-reviewed publication. **The report must be 25-50 pages**, use 1-inch margins, single spacing, and Arial size 12 font. Reports must be submitted electronically in non-protected Adobe Portable Document Format (PDF), and in accordance with the Federal Assistance Reporting Checklist and Instructions in the Award document. Documents are to be uploaded to the following DOE website:

https://www.eere-pmc.energy.gov/SubmitReports.aspx

Final reports that do not adhere to the above requirements are noncompliant and may affect cost reimbursement.

Due Date: Final reports are due no later than 90 days from the end of the project period. However, we request that they be submitted within 30 days in order to conclude the project in a timely fashion.

Final Report Template

Project Title:	Novel photon management for thin-film photovoltaics
Project Period:	10/01/12 – 08/14/16
Project Budget:	$449,814
Submission Date:	11/01/16
Recipient:	US Department of Energy
Address:	Energy Efficiency and Renewable Energy Golden Field Office, CO
Award Number:	EE0005959
Project Team:	University of Utah, Oak Ridge National Laboratory
Contacts:	Rajesh Menon USTAR Associate Professor, Dept. of Electrical & Computer Engineering, University of Utah Phone: 801-585-1058 Email: rmenon@eng.utah.edu

Executive Summary:

The objective of this project is to enable commercially viable thin-film photovoltaics whose efficiencies are increased by over 10% using a novel optical spectral-separation technique. A thin planar diffractive optic is proposed that efficiently separates the solar spectrum and assigns these bands to optimal thin-film sub-cells. An integrated device that is comprised of the optical element, an array of sub-cells and associated packaging is proposed.

A schematic of the proposed device is shown in Fig. 0. The polychromat is comprised of a specially designed microscale pattern that is created on the top surface of the cover-glass. The sub-cells in this example are comprised of two absorbers (shown in red and blue) both fabricated on a single rigid substrate. In the example shown, incident sunlight is split into two bands and concentrated by 2X; both functions can be achieved with optical efficiency of over 90% across the entire solar spectrum.

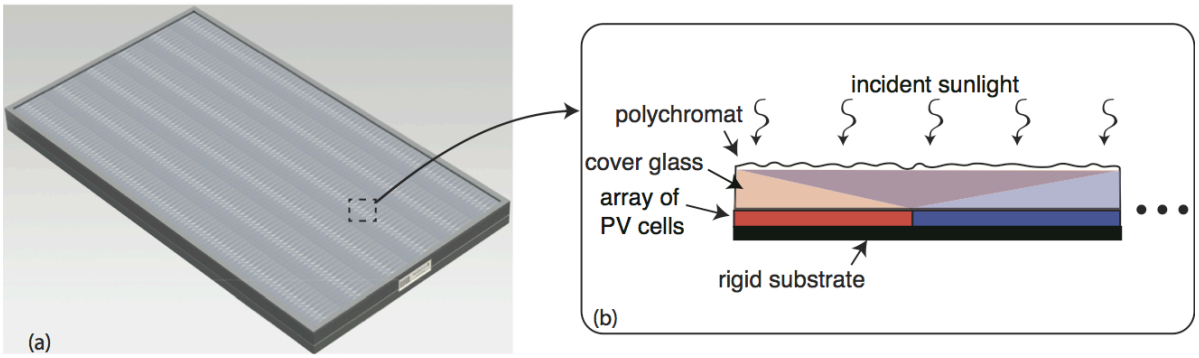

Figure 0: *The proposed module (a) is comprised of a parquette of repeating units. Each repeating unit (b) is comprised of a diffractive optic (polychromat) and an array of sub-cells. The polychromat spectrally splits and concentrates sunlight. No additional element is necessary as the polychromat can be incorporated into the top cover glass. Note that the optic may be 1D (as shown) or 2D. In this project, we will assume 1D designs.*

Key Findings:

We developed new computationally efficient methods and associated software for designing broadband diffractive optics such as the polychromat. We developed optimized fabrication procedures for manufacturing the polychromat including replication techniques. Related to this, we also indentified potential commercial vendors, who could manufacture the polychromat in the future. We built several prototypes that integrated the solar cells with the polychromats. Finally, we characterized these prototypes under a solar simulator and also under ambient sunlight, confirming the improvement in efficiency due to the spectrum splitting and concentration offered by the polychromat. The power improvements were 35.5% (3-cell device, solar simulator) and 25% (2-cell device outside). We encountered discrepancies between our experimental results and simulations. After detailed analysis, we attribute these discrepancies to fabrication errors as well as degradation of the polychromat over time. These problems can be solved in the future by going to commercial suppliers.

Table of Contents

Background:

Solar energy holds potential to become a significant source of energy in the near future [1]. The efficiency with which photons can be converted into charge carriers in a photovoltaic device is limited fundamentally by the Shockley-Queisser limit [2]. This upper bound arises from the fact that the solar spectrum stretches from ~350 nm to almost 2000 nm. Unfortunately, a single bandgap absorber is unable to convert all incident photons into charge carriers efficiently. Photons with energy below the bandgap are not absorbed at all, while photons with energy much higher than the bandgap tend to lose the excess energy (beyond the bandgap) rapidly as heat within the semiconductor lattice, a process commonly referred to as thermalization. Recent work in the optimization of photonic properties has allowed a thin-film GaAs photovoltaic device to reach ~85% [3,4] of its Shockley-Queisser limit of 33.5% [5]. It is widely acknowledged that achieving efficiencies beyond this limit could have a tremendous technological impact. As has been noted earlier, the primary loss mechanisms that need to be overcome are non-absorption and thermalization [6]. An effective approach is to separate the solar spectrum into smaller constituent bands and absorb these bands with band-matched absorbers. However, preconditioning of the incident sunlight to enable spectrum-splitting with conventional optical devices has proven to be impractical or inefficient. Spectrum-splitting using dichroic mirrors [7], beamsplitters [8] or prismatic elements [9] have been demonstrated. The main disadvantages of these approaches are their high cost, inability to scale to large areas and bulky configuration, making them unsuitable for practical solar applications. For dichroic mirror-based designs, other factors such as Fresnel reflection losses from multiple interfaces also limit their scalability to a large number of spectral bands. Holographic spectrum splitting is highly inefficient over the broad solar spectrum. Furthermore, they suffer from degradation under long-exposure to sunlight.

Nevertheless, the benefits of spectrum-splitting in photovoltaic devices have been demonstrated by vertically grown multi-junction solar cells [10-12]. Although an impressive efficiency of 43.5% at a geometric concentration of 418X has been achieved [3,13], their widespread adoption is stifled by the high cost of epitaxial growth and the complexity of metamorphic growth [12]. Furthermore, in such devices the individual absorbers are connected in series and hence, constrained to output the same current. This is problematic since the photon density in the corresponding bands of sunlight may not be the same for the different absorbers. Such a rigid constraint will reduce net energy yield due to the temporal variations in the solar spectrum [14].

References for Background:

1. Optics and Photonics: Essential Technologies for Our Nation, (National Research Council, 2012): http://www.nap.edu/catalog.php?record_id=13491
2. Shockley W, Quesisser HJ. Detailed balance limit of efficiency of p-n junction solar cells. *Journal of Applied. Physics* 1961; **32**: 510-519.
3. Green MA, Emery K, Hishikawa Y, Warta W, E. D. Dunlop ED. Solar cell efficiency tables (version 39). *Progress in Photovoltaics: Research and Applications* 2012; **20**: 12-20.
4. Record of GaAs solar cell from Alta Devices: http://www.technologyreview.com/news/424435/alta-devices-breaks-solar-cell-record/;
5. Miller OD, Yablonovitch E, Kurtz SR. Intense internal and external fluorescence as solar cells approach the Schockley-Queisser efficiency limit. *arXiv:1106.1603 [physics.optics]*.

6. Polman A, Atwater HA. Photonic design principles for ultrahigh-efficiency photovoltaics. *Nature Materials* 2012; **11**: 134-137.
7. Ruhle S, Segal A, Vilan A, Kurtz SR, Grinis L, Zaban A, Lubomirsky I, Cahen D. A two junction, four terminal photovoltaic device for enhanced light to electric power conversion using a low-cost dichroic mirror. *Journal of Renewable Sustainable Energy* 2009; **1**: 013106.
8. Mitchell B, Peharz G, Siefer G, Peters M, Gandy T, Goldschmidt JC, Benick J, Glunz SW, Bett AW, Dimroth F. Four-junction spectral beam-splitting photovoltaic receiver with high optical efficiency. *Progress in Photovoltaics: Research and Applications* 2011; **19**: 61-72.
9. Stefancich M, Zayan A, Chiesa M, Rampino S, Roncati D, Kimerling L, Michel J. Single element spectral splitting solar concentrator for multiple cells CPV system. *Optics Express* 2012; **20**: 9004-9018.
10. King RR, Law DC, Edmondson KM, Fetzer CM, Kinsey GS, Yoon H, Sherif RA, Karam NH. 40% efficiency metamorphic GaInP/GaInAs/Ge multijunction solar cells. *Applied Physics Letters* 2007; **90**: 183516.
11. Dimroth F, Kurtz S. High-efficiency multijunction solar cells. *MRS Bulletin* 2007; **32**: 230-236.
12. Geisz JF, Friedman DJ, Ward JS, Duda A, Olavarria WJ, Moriarty TE, Kiehl JT, Romero MJ, Norman AG, Jones KM. 40.8% efficient inverted triple-junction solar cell with two independently metamorphic junctions. *Applies Physics Letters* 2008; **93**: 123505.
13. Record of concentrated triple-junction solar cell from Solar Junction: http://www.sj-solar.com
14. Philipps SP, Peharz G, Hoheisel R, Hornung T, Al-Abbadi NM, Dimroth F, Bett AW. Energy harvesting efficiency of III-V triple-junction concentrator cells under realistic spectral conditions. *Solar Energy Materials and Solar Cells* 2010; **94**: 869-877.

Introduction:

Solar energy is not yet widely used due to its relatively high cost. Without government mandates, solar energy can be up to ten times more expensive than energy from coal. As the PV industry matures, some of these costs are expected to drop. However, in order to achieve grid parity, more will be needed. For instance, even if materials costs were zero (currently they make up ~54% of the total installed costs), grid parity cannot be achieved without considerable improvements in efficiency. Furthermore, increase in panel efficiency can also reduce installation and transportation costs due to the reduced number of panels required.

In conventional solar cells, when a photon of energy higher than the semiconductor bandgap is absorbed, charge carriers are generated. These charge carriers are separated in the junction and diffuse to opposite electrodes, generating an open-circuit voltage. When a load is connected to the cell, a current flows, generating electrical power. When the photon has energy smaller than the band-gap, it is not absorbed. When the photon has energy much larger than the band-gap, the extra energy is lost as heat in the crystal structure, referred to as the thermalization loss. As a result, energy within a significant portion of the solar spectrum is wasted. These two losses along with the intrinsic radiative recombination loss account for almost 70% of total energy loss. Multi-junction solar cells were invented to overcome these losses. However, these are extremely expensive. Furthermore, they have several technical disadvantages, which limit their applicability, including: (1) The lowest current in the series connection limits the total current from the multi-junction cell. Since the maximum power operating point of each material (bandgap) is different, this effectively constrains the cells to operate sub-optimally; (2) Due to the complexities of lattice matching different materials, it is extremely difficult to have more than 3 bandgaps in a practical multi-junction cell; (3) Multi-junction cells require special care in designing tunnel

junctions that connect the cells in series. Optical transparency (wide band-gap) and low electrical resistance are generally incompatible requirements.

Our solution to overcome these limitations is by incorporating a novel optic (which we call a *polychromat*) that not only concentrates sunlight, but also spectrally separates and assigns the different spectral components to solar sub-cells with bandgaps that line up with the incident spectra. A schematic of the proposed system is shown in Fig. 1. The polychromat is distinct from a grating or a prism. With a grating or prism, concentration is not possible without a second optic. Moreover, the locations of the spectral bands are not readily controlled. The diffraction efficiency of a grating over the solar spectrum is typically very poor (less than 10%). Finally, the prism is not scalable to large areas since its volume and hence, weight will become impracticably large.

Cost of Power: We performed an analysis of the cost of power generated using the proposed approach via a simplified cost model. The cost per peak power generated is given by:

$$\text{cost} = \frac{C_{conc} + \frac{\langle C_{cell} \rangle}{G} N_{cells} + C_{parts}}{P\eta},$$

where C_{conc} is the cost per unit area of the concentrator, $\langle C_{cell} \rangle$ is the average cost per unit area of the photovoltaic sub-cells, N_{cells} is the number of photovoltaic sub-cells, C_{parts} is the cost per unit area of everything else in the panel, G is the geometric concentration factor (assumed to be the same for all the sub-cells), P is the direct solar insolation (W/m^2), and η is the power-conversion efficiency.

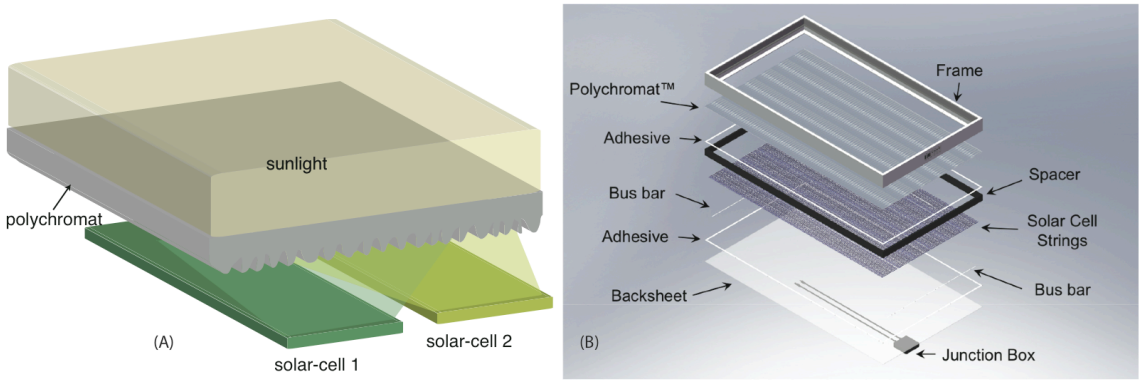

Fig. 1: *(A) Schematic of proposed device. The device consists of the polychromat and an array of solar sub-cells (2 shown here). When the polychromat is designed to be 1-D (as shown), daily sun-tracking is not required. Improved designs using angle-multiplexing approaches can avoid tracking altogether within the limits of étendue conservation. When the spectral bands match the band-edges of the solar sub-cells, efficiency is increased dramatically.(B) Schematic of a panel that will incorporate the polychromat and sub-cell arrays.*

The photovoltaic material costs usually dominate the balance of system costs in solar-energy extraction. However, this cost is significantly reduced with thin-film materials. In addition, with higher efficiency, the cost per watt goes down dramatically. Increasing the concentration can considerably reduce this cost. However, to avoid the cost of tracking, we will only focus on low concentration solutions (less than 10X). Assuming η = 26% and N_{cells} = 2, the cost per power generated will be ~ **32 ¢/W** at a concentration of 4X. Although this model is highly simplistic, it is clear that the proposed approach has the potential to generate electricity from sunlight at prices that are lower than with conventional approaches (*i.e.,* less than ~$1/W), while still maintaining high device efficiency. The other key assumptions are C_{conc} = $10/m^2, $\langle C_{cell} \rangle$ = $50/m^2, C_{parts} = $50/m^2 and P = 1000 W/m^2. At higher efficiencies (with more spectral bands), the corresponding cost per watt goes down as the extra sub-cells are made of inexpensive thin-film materials.

The Polychromat: The polychromat is a microfabricated broadband optic that not only concentrates sunlight but also separates the spectral components. Being a generalized broadband computer-generated hologram (CGH), the polychromat is comprised of a carefully designed 3-D surface topography as illustrated in Figs. 2(A) and (B). The PI, Menon has developed unique algorithms that enable the design of such optics.[11] These algorithms are based on enumerative modified error-reduction techniques and require special care for computational scalability. The PI and students have recently demonstrated the scalability of these algorithms with a modified perturbation approach that can be readily parallelized using graphical-processing-unit (GPU) architectures. The second challenge here is the fabrication of such optics. The PI has developed novel grayscale lithography techniques that enable the fabrication of these elements over large areas as illustrated in Fig. 2. For manufacturability, we will constraint the feature sizes of these optics to greater than 1mm. This will also allow us to explore the applicability of roll-to-roll processing techniques for low-cost manufacturing. Fig. 2(C) shows the optical performance of one polychromat that was designed as a visual cue – to separate the visible spectrum into red and blue bands. The measured optical efficiency agreed very well with the predicted one. Significant research needs to be conducted to extend these optics to allow for the collection of larger input angles (via angle multiplexing) while still being within the étendue-conservation limit of $\sin^{-1}(1/G)$ ~ 14 degrees for 4X concentration.

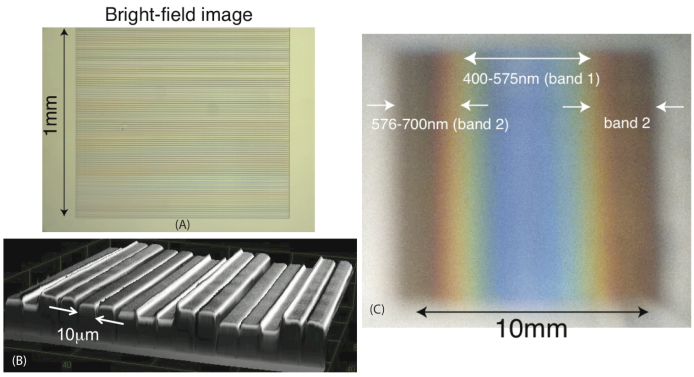

Fig. 2: *Preliminary experimental results of the polychromat. (A) Bright-field image of a 1-D polychromat. (B) Magnified optical profilograph of the same polychromat showing*

the multiple levels and 10mm minimum features. (C) The image plane of the polychromat when illuminated by white light. The visible spectrum is separated into a central blue band and two symmetric red bands. This is only for visual demonstration.

The sub-cells: The solar sub-cells in the proposed configuration have very special requirements, namely that their bandgaps can be tailored readily and that they should be inexpensive. Heterojunctions of III-V materials are well-known for having customizable bandgaps. However, these are expensive and are economically viable only for high concentration. Thin-film materials are very attractive for the proposed system. In fact, various groups have clearly demonstrated that thin-film materials (CIGS and other chalcogenides) can be tailored for multiple bandgaps. Lee and co-workers have also developed novel technologies for the robust fabrication of such photovoltaic sub-cells. An image of a very preliminary sub-cell pair using this approach is shown in Fig. 3(A). A parquette of such pairs would be coupled with a parquette of polychromats as illustrated in Fig. 1(B). Preliminary electrical characterization of a single sub-cell pair with one polychromat has been completed. As indicated in Fig. 3(C), the peak power of each sub-cell is maximized when the spectral bands are spatially aligned with the sub-cell boundaries.

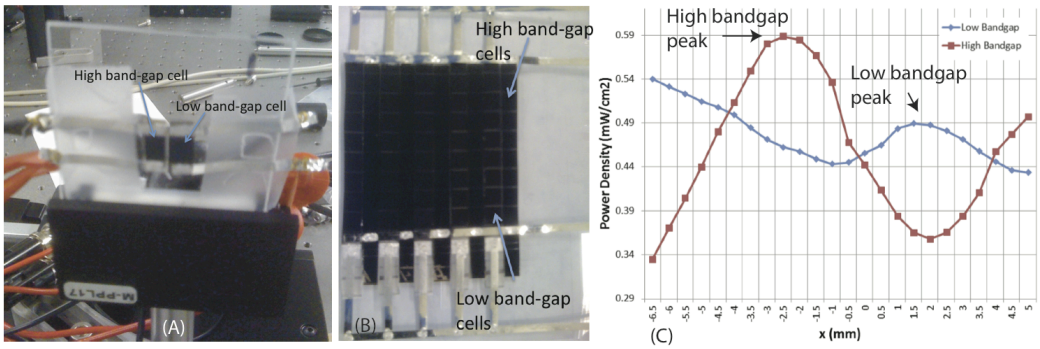

Fig. 3: *Preliminary characterization results. (A) A single sub-cell pair comprised of a high bandgap and a low bandgap cell. (B) A parquette of high- and low- bandgap cells, which could be integrated with a corresponding array of polychromats. (C) Peak power output as a function of position of the sub-cells. Note that each sub-cell peaks at the designed location, where the spectral band matches the sub-cell boundaries. The low-bandgap output decreases slightly towards the left due to the non-uniform illumination.*

The milestones of the project were:

1. Publications describing the process for fabricating the prototype and its measurements.
2. Invention disclosures describing the processes for fabricating the integrated device and incorporating the polychromat.
3. Measurement data that shows conclusively that spectrum splitting with the polychromat allows for at least a 10% increase in power output from the integrated device (size ~ 0.5cm X 0.5cm) compared to a single bandgap control device under no spectrum split conditions.

Project Results and Discussion:

Fabrication and Characterization of the polychromat.

The objective of this task was to take the photoresist pattern of the polychromat and convert it into a replicated pattern within a transparent material (transparent to the entire solar spectrum). We originally proposed creating this pattern in glass. We subsequently realized that it is much simpler and cheaper to replicate the pattern in a transparent plastic. If we can then utilize solar grade plastic such as solar-grade poly-methyl-methacrylate (PMMA), we could realize a cost-effective manufacturing process based upon stamping. Our main achievements along this goal are described below.

Master Pattern: The polychromat master pattern was fabricated using grayscale lithography on a thin film of commonly used Shipley 1813 photoresist. An optical micrograph of the fabricated optic is shown in Fig. 14(a). The inset in the figure shows an atomic-force micrograph of a small portion of the optic delineated by the white square. This image confirms the height distribution and the width of the pixels. We measured the standard deviation of the errors in pixel-heights due to fabrication errors as about 100 nm.

Optical Characterization of Master Pattern: The polychromat was optically characterized by measuring the spectral characteristics of its diffraction pattern at the image plane that is 120mm away from the polychromat. The resulting spectral transmission efficiency is shown in Fig. 14(d). The transmission or optical efficiency is calculated as the total power at the image plane integrated over the left or right absorber area, respectively, and divided by the total input power integrated over the entire polychromat area. In contrast, the system efficiency refers to the total electric power of the combined cells divided by the incident light power. The numerical simulation (solid lines) shows that the average optical efficiency is 85%. The measured efficiency is also shown (dashed lines) and has an average efficiency of 75%. They are both mean values of the optical efficiencies within the two spectrum bands: high-energy band (averaged from 400nm to 630nm) and low-energy band (averaged from 630nm to 900nm). The reduction in efficiency for the measured polychromat was the result of a combination of errors introduced during fabrication in the pixel heights (~100 nm) and errors in the dispersion data of the photoresist. A second numerical simulation was ran including these height and dispersion errors (dotted-dashed lines) resulting in a much better match between our numerical model and the measured data. In addition, a spatial-spectral image map was created for the original simulation by the Fresnel transform[10] and the measured data and is shown in Fig. 14(c) and Fig. 14(b) respectively, which also demonstrate excellent agreement. The spectrally-integrated intensity distribution was calculated to show that the image is reasonably uniform across the entire solar cell surfaces. However, if further uniformity is desired, our design algorithm can be readily modified to incorporate this requirement. The illumination was spatially collimated white light from a Xenon lamp (More recently, we have made a setup with a super-continuum source, which offers a significantly flatter spectrum). As expected, the high-energy photons are localized to the left half of the image plane, while the low-energy photons are redirected to the right half.

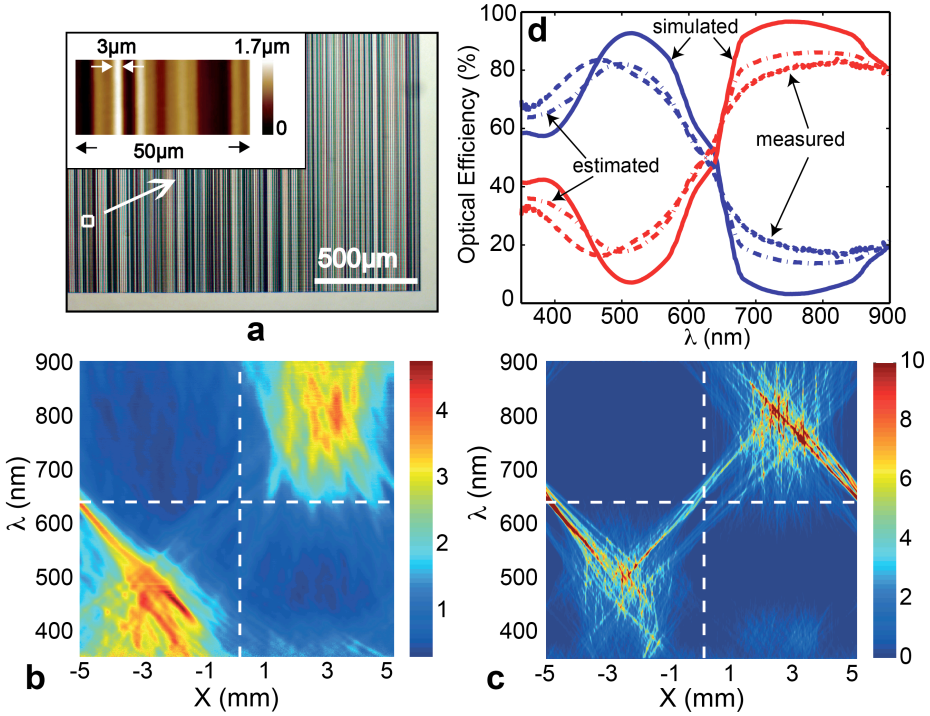

***Figure 14**: Polychromat design and optical characterization results. (a) Microscopic image of the designed and fabricated polychromat with back illumination (Inset: atomic-force micrograph of a small portion of the polychromat delineated by the white block). Spatial-spectral intensity distribution at the image plane measured (b) and simulated (c). (d) Spectral efficiency of the polychromat for the two bands. Blue lines are for the GaInP cell and red lines are for the GaAs cell. Solid lines are from simulations of the designed polychromat, dashed lines are from real measurements, and dotted-dashed lines represent estimations by considering the corrected dispersion data of Shipley 1813 photoresist and fabrication error with standard deviation of 100nm.*

Electrical Characterization: As the next step, we simply utilized the master pattern (in photoresist) to electrical characterize two discrete solar cells (GaAs and GaInP). The solar cells were characterized independently by measuring their current-voltage curves under conventional illumination (reference, without polychromat) and spectrum-split illumination (with polychromat), both using the same source. As shown in Fig. 15(a), spectrum-splitting with the polychromat increases the short-circuit current-density of the GaInP cell by 58% (simulation) and by 26% (measurements). This can be understood by the increase in the high-energy photons that are redirected towards the GaInP cell by the polychromat. In the reference case, such photons that land on the right-hand side of the image plane completely miss the GaInP cell (which is placed on the left-hand side of the image plane). The open-circuit voltage of the GaInP cell shows an increase of 7% (simulation) and of 4% (measurements) likely due to the increased photon flux.[11] On the other hand, the GaAs cell (which is placed on the right-hand side of the image plane), loses the re-directed high-energy photons compared to the reference. Although, some of the low-energy photons are re-directed towards the GaAs cell by the polychromat from the left-hand side of the incident beam, the overall effect is such that the short-circuit current-density of the GaAs cell increases by 5% (simulation) and by 13%

(measurements) as shown in Fig. 15(b). Its open-circuit voltage also increases slightly by 2.3% (simulation) and by 2.9% (measurements). The fill-factors of both the cells are maintained during spectrum-splitting. As a result, the power-density of both cells show increase as illustrated in Figs. 15(c) and 15(d). The simulations predict the peak-power-density of the GaInP cell to increase by 69% and that of the GaAs cell to increase by 7.7% under spectrum-split illumination compared to the reference. The measured peak-power-density increase for the GaInP and the GaAs cells are 29% and 16%, respectively. The combined power-density from both cells under spectrum split conditions is predicted to increase by 26% and the corresponding measured increase is 20%. When the total power under spectrum splitting is compared to power output from a single GaAs cell of the same area as the polychromat, we notice that there is no improvement from spectrum splitting. However, this isn't an inherent problem with spectrum splitting, but rather a problem arising from the huge spectral overlap in the external quantum efficiencies of the two cells that we used. By choosing optimal solar cells, the improvement due to spectrum splitting will be significant even when compared to one of the cells without spectrum splitting, as has been noted previously.[11]

The discrepancies between simulation and measurement in device power output are primarily due to fabrication errors that degrade the polychromat transmission performance as discussed earlier. Specifically, as can be seen in Fig. 14(b), the optical efficiency of the polychromat is reduced in the spectral range from 460 nm to 620 nm, which includes a significant portion of the input light spectrum. This means that some of the high-energy photons, which should have been redirected to the GaInP cell are now incident on the GaAs cell. Thereby, the GaInP cell exhibits a smaller-than-expected and the GaAs cell shows a larger-than-expected increase in their respective short-circuit-current densities. By using the measured optical efficiency spectrum of the polychromat, we can estimate the electrical characteristics of the two cells as illustrated by dotted lines in Fig. 10. This estimation agrees well with the measured characteristics, thereby validating our optoelectronic model.

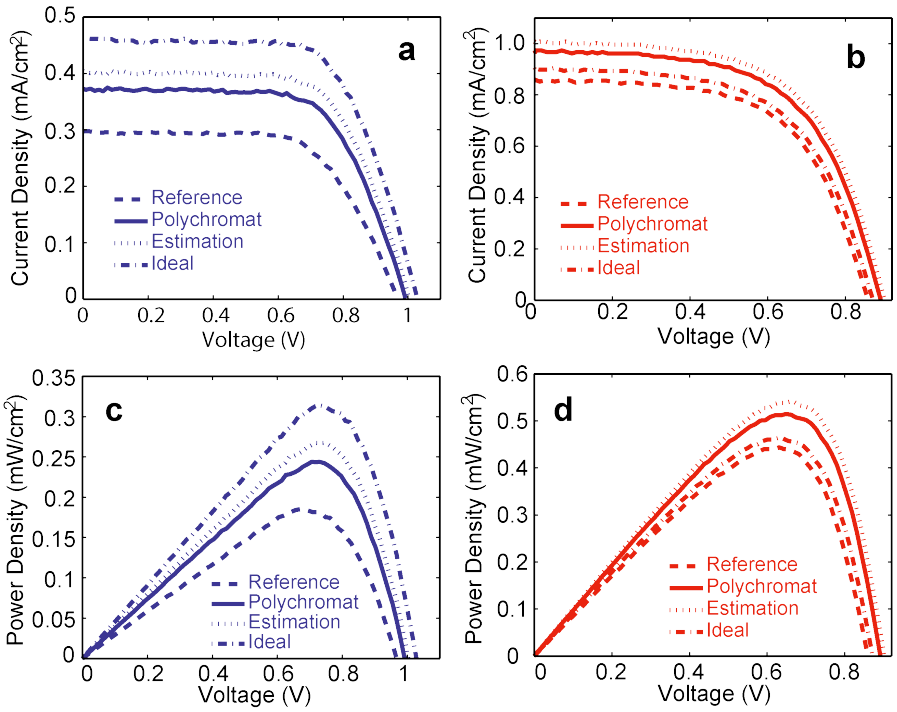

***Figure 15**: Electrical measurement results. (a) J-V curve of the GaInP cell. (b) J-V curve of the GaAs cell. (c) P-V curve of the GaInP cell. (d) P-V curve of the GaAs cell. Solid lines are derived from measurements with spectrum-splitting by polychromat. Dashed lines stand for reference measurements without polychromat. Dotted lines are simulation results estimated by considering the measured spectral efficiencies. The simulated ideal cases with the designed polychromat are represented by dotted-dashed lines.*

Replication into Daughter Patterns: Next, we invested our efforts in developing a robust process to take the master pattern in photoresist and convert it into replicated patterns in a transparent plastic. We chose the process sequence illustrated in Fig. 16, where the master pattern is first replicated using a PDMS moulding process, and then the PDMS mould is used to imprint the pattern into polystyrene.

For the Poly(dimethylsiloxane) (PDMS) mould, we used Sylgard 184 Silicone Elastomer Kit from Dow Corning. A disposable plastic container was placed on a scale and silicone elastomer base and curing agent were poured in a 10:1 (base:curing agent) weight ratio. Silicone elastomer base and curing agent were mixed vigorously by hand using a plastic fork for about 5 mins. The mixture was poured onto the substrate (which was wrapped with aluminium foil). The substrate (with PDMS mixture on top of it) was placed in a vacuum desiccator for about 30 mins. The substrate was then placed in an oven at 60 degree C for 5 hours to cure PDMS. Finally, a razor blade was used to peel the cured PDMS off the substrate.

For the Polystyrene sample, we simply 4” circular pieces out of a polystyrene petri dish. We utilized the bonding tool ‘EVG 520 IS’ available in the Utah nanofab for thermal imprinting. PDMS mold was placed on the polystyrene sample and these two were sandwiched between two 4” silicon wafers (one on the top of PDMS mold and another at the bottom of polystyrene). This whole stack was placed on the chuck of the

bonding tool. The sample was heated to 110degC and a maximum force of 1700N was applied using a piston for 5 minutes. After cooling, the piston was raised and the sample separated from the mould. The resulting sample is shown in Fig. 16.

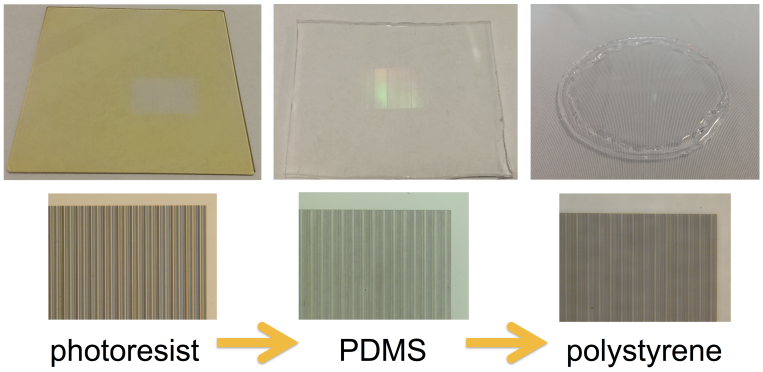

***Figure 16**: Replication process from photoresist master to PDMS mould to polystyrene daughter pattern. Corresponding micrographs are shown on the bottom.*

In order to characterize this process, we used the atomic-force microscope to measure a few randomly chosen polychromat pixels at each stage of the process. The resulting data is summarized in Table 1 below.

Table 1: Atomic-force microscope measurements of fabricated samples.

Pixel number	Depth on photoresist (nm)	Depth on PDMS (nm)	Difference between depths on photoresist and PDMS (nm)	Depth on polystyrene(nm)	Difference between depths on PDMS and polystyrene (nm)
1	1170	1109	61	949	160
2	998	947	51	828	119
3	693	641	52	584	57
4	480	441	39	403	38

The maximum error we measured was 160nm, much smaller than the wavelengths of interest. Therefore, we believe that this process will be very robust. As next steps, we will optical characterize these replicated patterns.

Our original idea was to take the photoresist master pattern and replicate this pattern into a glass substrate. However, we quickly realized that it is much simpler and cheaper and equally effective to replicate the master pattern into a transparent plastic instead. Although glass would be, in principle more robust than plastic, there are commercial solar-grade plastics such as PMMA from a variety of companies such as Evonik etc. For example, the plastic, Acrylyte Solar 0Z023 is marketed as a highly weather resistant and extremely transparent version of PMMA. Since such a material will be much cheaper to manufacture and lighter to transport, we decided to modify the subtasks 3 and 4 to replicate the master pattern into a transparent plastic. Furthermore, such optics is quite routinely manufactured in large volumes using roll-to-roll embossing processes

primarily for applications in lighting, displays, etc. We decided that we could take advantage of this existing knowledge base and infrastructure to readily transfer our process into high-volume manufacturing in the future. The details of our process were described earlier. In summary, we successfully took the photoresist master pattern and made a PDMS mould of it. Then, the PDMS mould was used to emboss the pattern into a polystyrene substrate using thermal embossing. We used atomic-force microscopy to carefully characterize the accuracy of this process as described earlier. We still have additional optimization of the replication process to be completed, namely the conditions for the PDMS mould as well as the temperature and pressure during the embossing process. Nevertheless, we have substantially accomplished the goals of the 2 subtasks listed here.

Since we require cells with different bandgaps for the prototypes, the ORNL team decided to pursue two different approaches to make the cells and then integrate them together as described below.

Fabrication of integrated sub-cells (by inkjet printing).

The inkjet printing of the polymer and metal thin films were carried out in a Dimatix DMP-2800 series materials printer (Fig. 4). The DMP-2800 series printer allows the deposition of fluidic materials on an 8×11 inch or A4 substrate, utilizing a disposable piezo inkjet cartridge. This printer can create and define patterns over an area of about 200 × 300 mm and handle substrates up to 25 mm thick with an adjustable Z height. The temperature of the vacuum platen, which secures the substrate in place, can be adjusted up to 60°C. The DMP-2800 offers a variety of patterns using a pattern editor program. Additionally, a waveform editor and a drop-watch camera system allows manipulation of the electronic pulses to the piezo jetting device for optimization of the drop characteristics as it is ejected from the nozzle. The inkjet system employs a MEMS-based cartridge-style printhead that allows users to fill their own fluids. To minimize waste of expensive fluids, each cartridge reservoir has a capacity of 1.5 ml. Cartridges can easily be replaced to facilitate printing of a series of fluids. Each single-use cartridge has 16 nozzles linearly spaced at 254 microns with typical drop sizes of 1 and 10 picoliters.

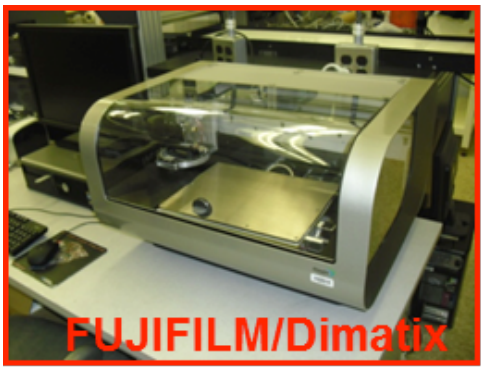

Fig. 4: *Dimatix inkjet materials printer.*

Ink Development: The inkjet printing technique was used to define additive integration of high performance polymer solar cells exploiting the spectrum splitting schemes. For inkjet printing, the polymer inks ere developed to meet the surface tension and viscosity requirements for high quality thin films. The solvent-selection and polymer-content control are two key variables for tailoring the ink characteristics for high performance thin film development. The printing of the active layer and contact-electrodes will be carried out at low temperatures suitable for polymer solar cell integration. The details of the thin film development and device characteristics will be presented in future reports.

Polymer PV Cells: In order to develop the fabrication process of integrated sub-cells for spectrum splitters, two conducting polymers were selected to define high and low bandgap absorbers. As shown in Figure 5, a typical polymer absorber, poly(3-hexylthiophene) (P3HT, $E_g \approx 1.9$ eV) absorbs at shorter wavelengths below 600 nm while PTB-7 conducting polymer ($E_g \approx 1.4$ eV) shows high absorption in the wavelength range of 600-900 nm. The bulk heterojunction polymer solar cells will be first fabricated with a target efficiency of about 4% for P3HT/PCBM subcells and 6% for PTB7/PCBM subcells. These low- and high-bandgap subcells will be integrated on patterned ITO/glass substrate by spin-coating technique to optimize the processing parameters (concentration, solvent and film thickness morphology) in environmental-controlled glove box system. The optoelectronic properties (absorption, photoluminescence) and thin film morphology of polymer blends will be characterized by optical spectroscopy and AFM.

We were able to process a 100-nm-thick P3HT/PCBM thin film by optimizing the spin coating process, and the corresponding PV cell shows >4% efficiency. The next step in our development is to fabricate low bandgap polymer subcells of PTB7/PCBM solar cells.

Polymer solar cells were developed using two different absorber materials: poly(3-hexylthiophene) (P3HT, Eg≈1.9 eV) and PBDTT-DPP (Eg≈1.4 eV). Those polymers were blended with [6,6]-phenyl-C71-butyric acid methyl ester (PC71BM, an electron-acceptor material) to make sub-cells, which can incorporate the spectrum-splitter at two ranges 300-600nm and 600-900 nm. The typical performance of the low- and high-bandgap sub-cells of polymer PV is shown in Fig. 6. The solar cell devices based on wide bandgap P3HT polymer and PCBM were fabricated by spin –coating method and the PCE was around 4.1%. The solar cell devices based on low bandgap PBDTTT-C-T and PCBM showed a PCE value of about 7.1%. The cells were shipped to University of Utah for the evaluation of spectrum splitting concept. However, the cell performance had degraded by the time electrical measurement setup was ready for testing. Due to these degradation problems, we decided not to pursue the OPV cells further.

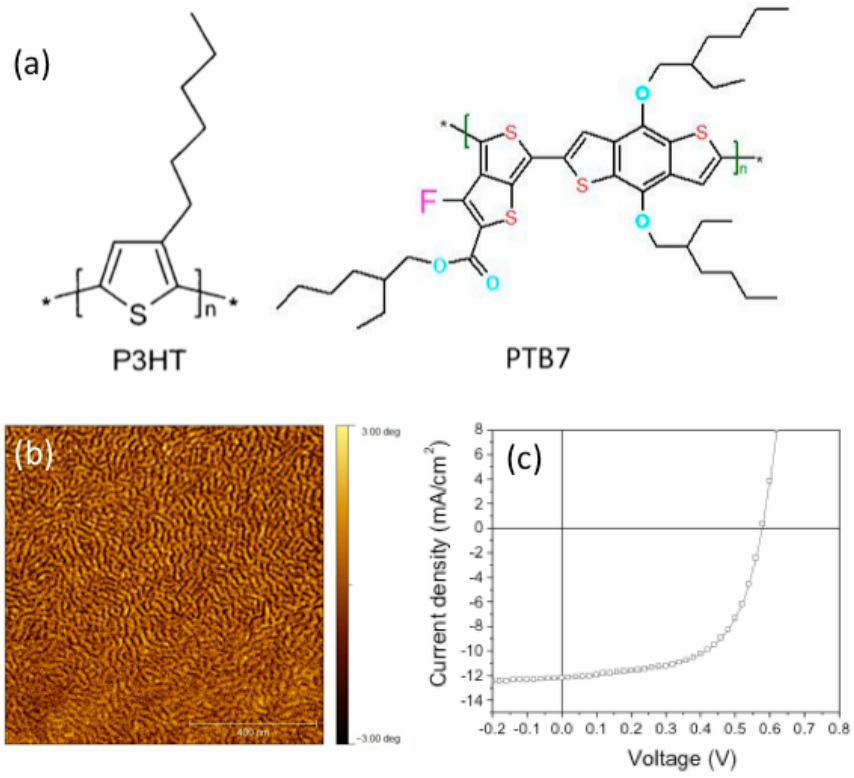

Figure 5: *(a) The typical polymer absorbers of P3HT and PTB7; (b) AFM image of spin-cast P3HT/PCBM film; (c) the current-voltage curves of P3HT/PCBM solar cells (V_{oc}, 0.58V, J_{SC}, 12.2 mA/cm^2, η, 4.2%).*

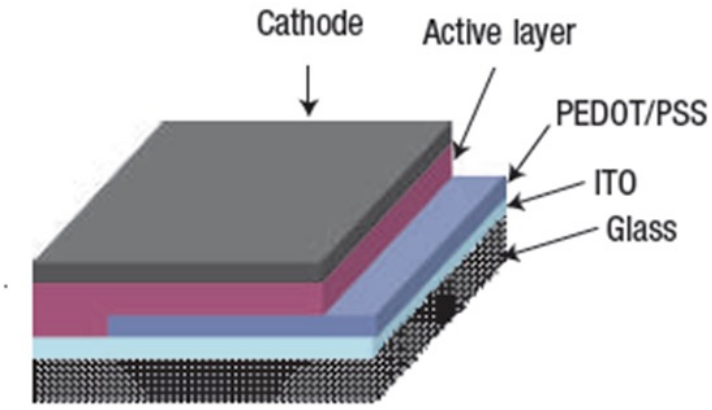

(a)

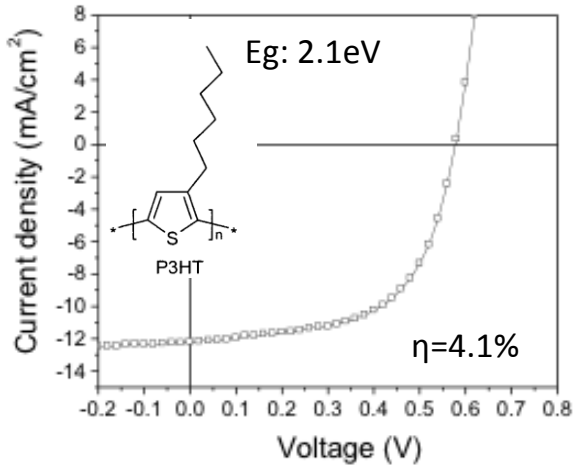

(b)

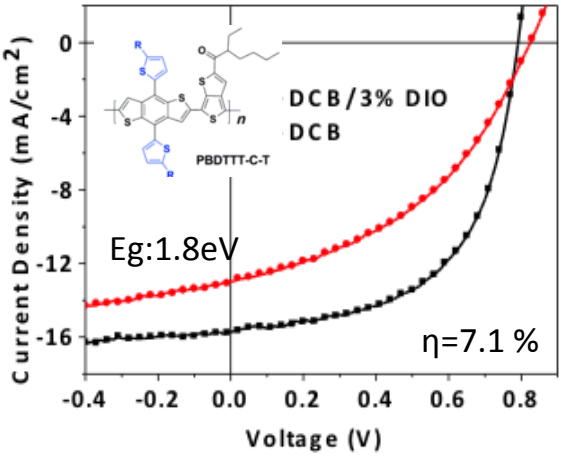

(c)

***Figure 6**: (a) A schematic of the polymer solar cell, and the photovoltaic device performances of (b) wide bandgap and (c) low bandgap polymers.*

Printed CIGS Development: CIGS nano-powders corresponding to bandgap of 1.0 eV and 1.5 eV were purchased (Xumatic Inc.) for the development and evaluation of printed CIGS absorber layer. Figure 7 shows the surface morphology and the crystallinity of the as-received powder samples which were screen-printed on various substrates. The coatings of 1.5 eV material showed the presence of Ga2Se3 and Cu2Se phases in addition to Cu(In0.3Ga0.7)Se2 phase. The Ga2Se3 phase was not observed for 1.0 eV bandgap material as shown in Figure 8.

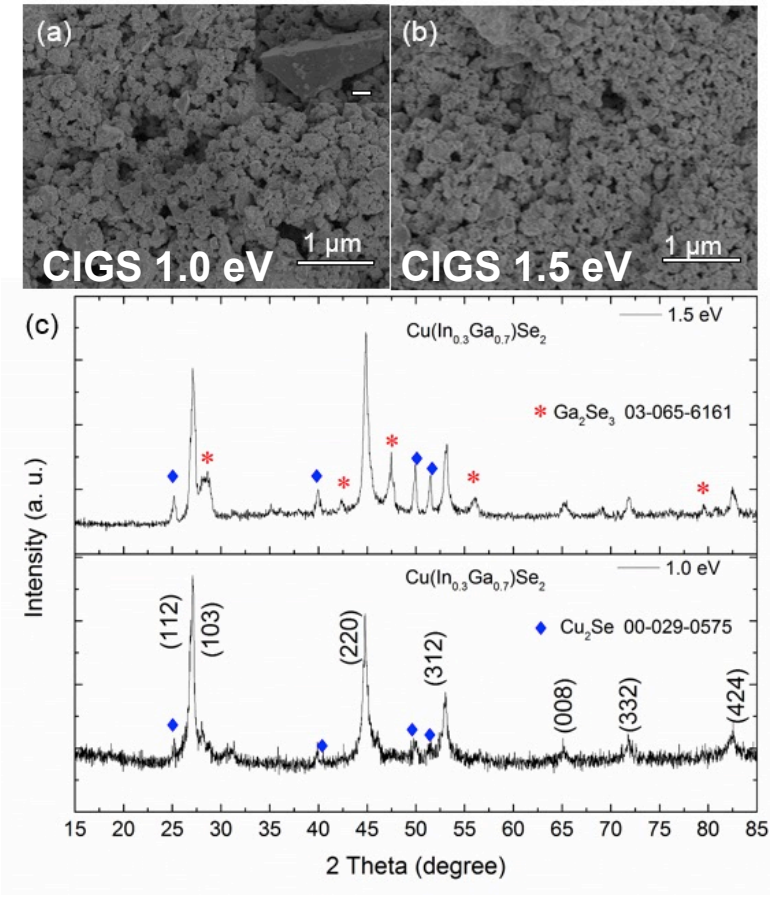

***Figure 7**: Surface morphology of the screen-printed CIGS nanoparticle coatings corresponding to a material bandgap of (a) 1.0 eV, and (b) 1.5 eV, and (c) crystallinity of as-printed films.*

Figure 8 shows the impact of furnace annealing on the microstructure of CIGS nanoparticle coatings. A typical annealing cycle is also shown in Figure 8(a). The grain growth, as shown in Figure 8(b), was found to be limited for the samples annealed in an inert atmosphere. However, annealing in Se atmosphere was effective in enhancing the grain growth for both the materials. A significantly larger grain growth was observed for the wider bandgap material. The x-ray diffraction measurements, as shown in Figure 5(c), indicated significant improvement in the film crystallinity after selenization for both the materials (1.0 eV and 1.5 eV bandgaps). However, the phases were not pure indicating that extensive effort is required to control grain growth while minimizing or suppressing the formation of secondary phases. The nanoparticle vendor showed limited flexibility in tailoring the material composition and could not provide information on the material composition or chemical synthesis technique used for processing. We could pursue in-house synthesis of CIGS nanoparticles. Due to fabrication challenges, we decided to pursue the prototypes using existing cells.

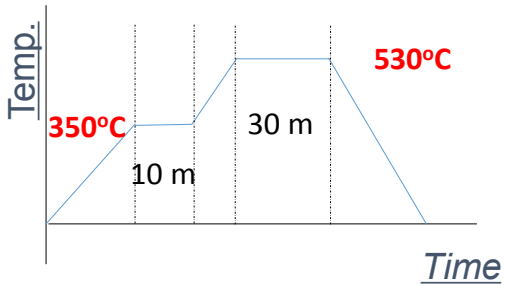

(a)

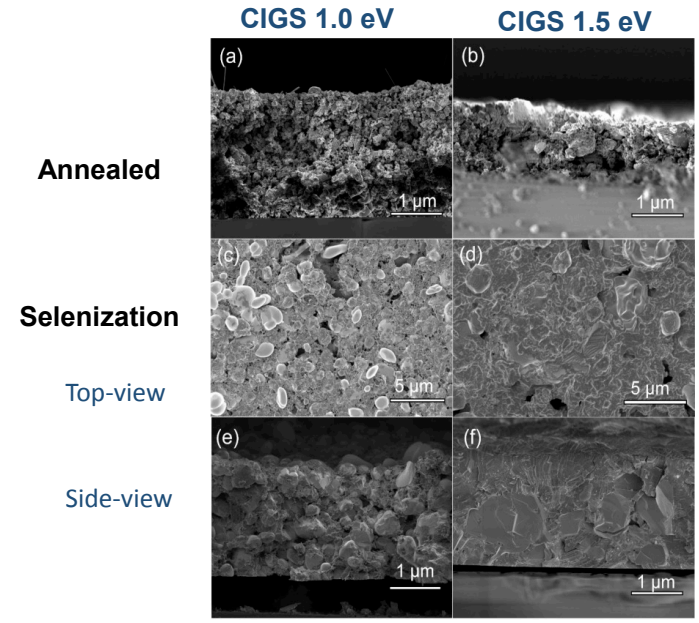

(b)

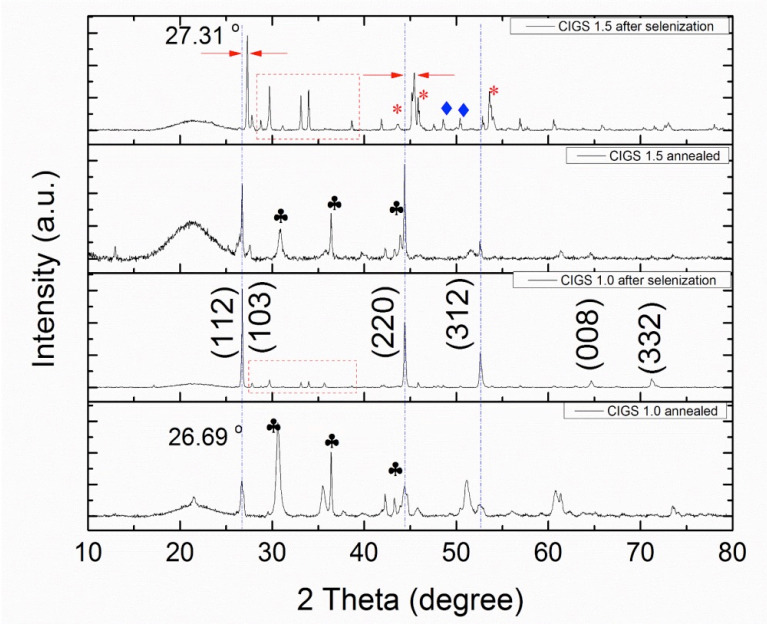

(c)

***Figure 8**: (a) Annealing cycle, and the impact of annealing on the (a) microstructure and (c) crystallinity of CIGS nanoparticle coatings.*

Fabrication of integrated sub-cells (by evaporation).

Absorber thin film fabrication: For the fabrication of absorber films, an intermixing approach is being investigated, where sequential deposition of single (e.g., Cu) and binary (e.g., GaSe and InSe) compositions of elements that comprises the CIS and

CIGS absorber layers were accomplished first by rf-magnetron sputtering from alloy targets at a substrate temperature of 400^{o}C followed by selenization treatment via IR-rapid thermal annealing (RTA) method in a graphite crucible (see Fig. 9) using a ramping rate of 100 ^{o}C/min. This approach allows us maximum flexibility to address any issues of inter-mixing of layers and also allows for the optimization of the absorber material parameters for best performance.

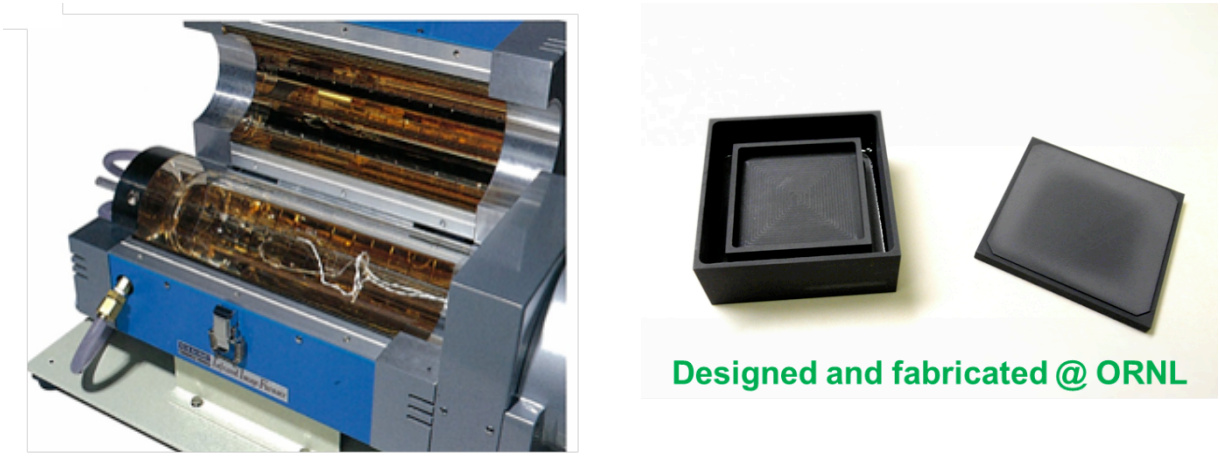

(a) (b)

***Figure 9**: (a) IR rapid thermal annealing system, and the graphite crucible used for annealing investigation.*

Typical θ-2θ X-ray diffraction (XRD) patterns of as-deposited precursor Cu/InSe and films after selenization on Mo/borosilicate substrates are shown in Figs. 10(a) and 10(b), respectively. Along with molybdenum and low-intensity CIS reflections, while Fig 10a displayed weaker peaks indexed for partially reacted secondary InSe and Cu_2In_3 phases, after the IR-RTA selenization well-defined CIS films were obtained as evidenced by the sharper CIS reflections along with the disappearance of secondary phase reflections. Note that, post-treatment processing of CIS and/or CIGS thin films using IR-RTA technique is essential in order to minimize damage and defect densities (i.e., recombination centers) in the near surface junction region, which in turn helps to improve the cell performance. The planar and cross-sectional SEM micrographs presented in Fig. 11 clearly displays the positive influence of IR-RTA process on the attainment of a dense film microstructure with large CIS grains, where each grain faces other grains without significant spatial gaps.

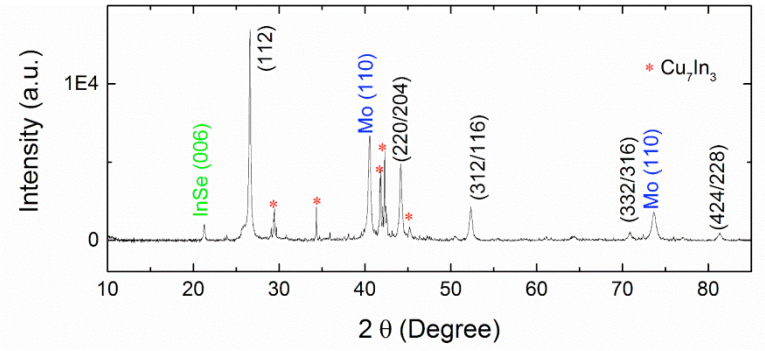

(a)

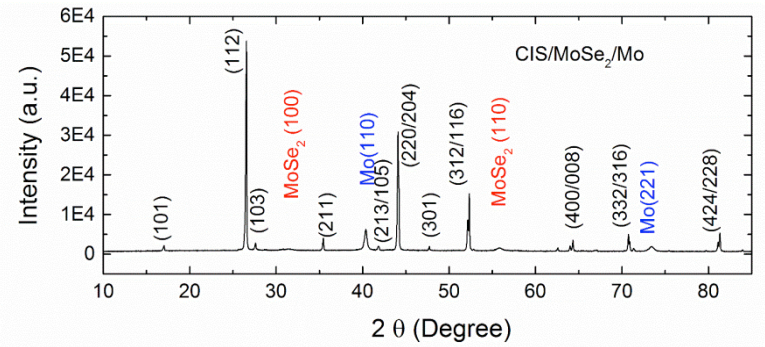

(b)

***Figure 10**: The θ-2θ XRD scans of sequentially sputter deposited Cu/InSe films on Mo/glass substrates a) before and b) after the IR-RTA selenization step.*

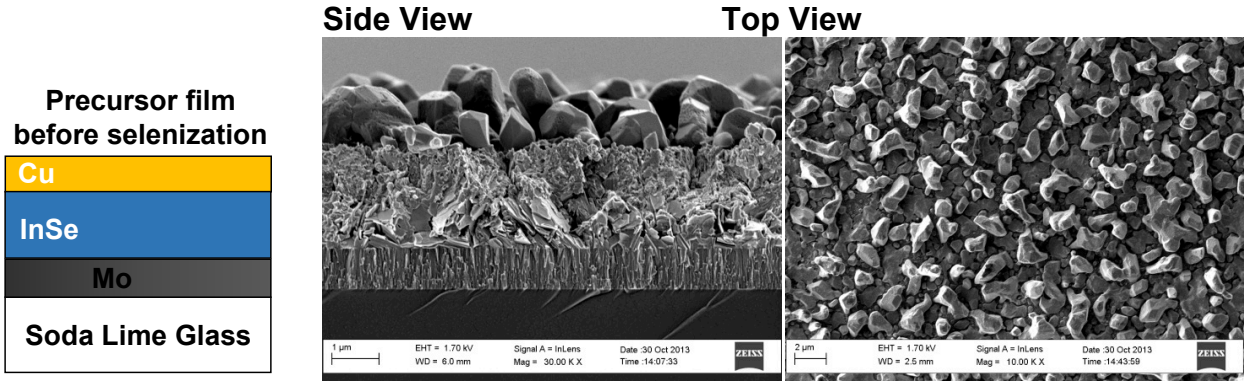

(a)

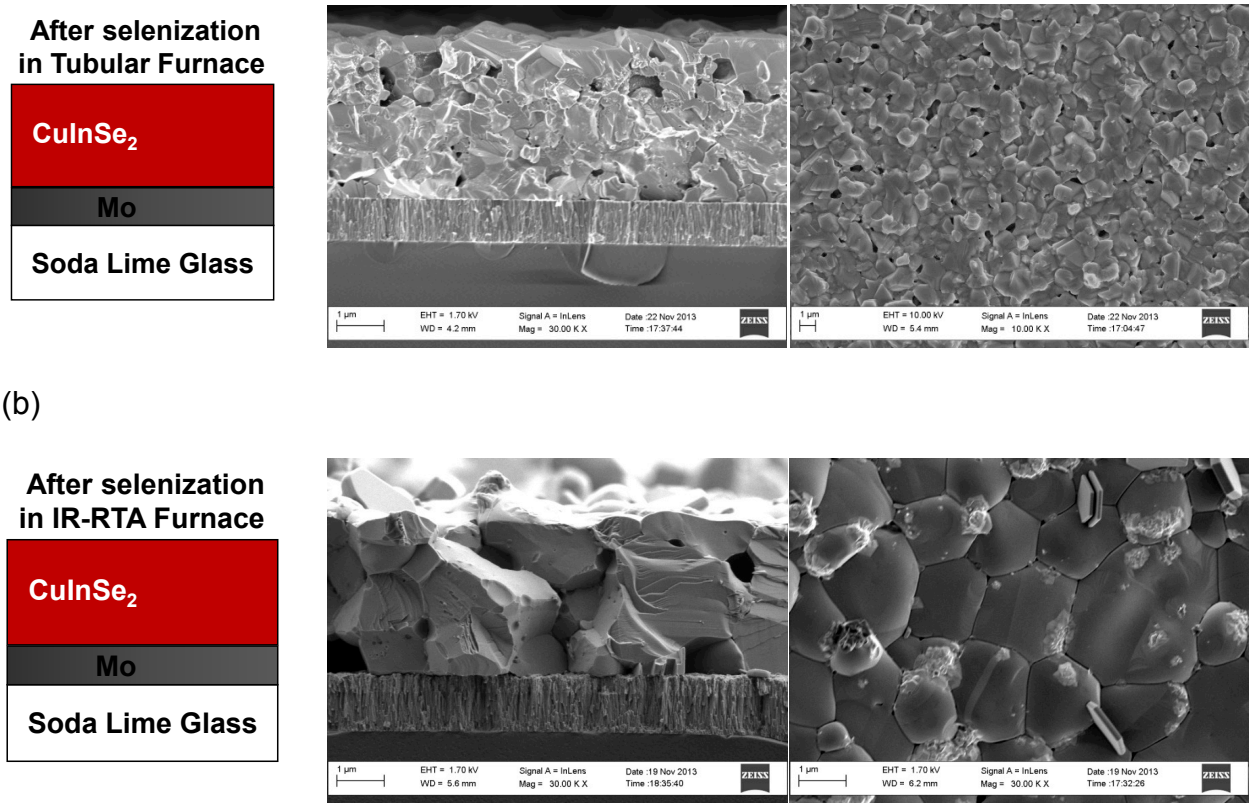

***Figure 11**: Typical design schematic of a CIS thin film structure and planar-view/cross-sectional SEM images: (a) as-deposited film, (b) films selenized in tubular furnace, and (c) films selenized in an IR-RTA system.*

Window layer fabrication: For the fabrication of subsequent window and transparent electrode layers, two approaches are being considered. The first approach involves sequential sputter deposition of *n-type* ZnMgO (buffer), ZnO (window), and Al doped ZnO electrode stack. Here ZnMgO serves as a buffer layer to optimize conduction-band alignment at the interface and ZnO:AlZnO bi-layer minimizes the sputtering induced defects and dislocations caused during the deposition of ZnO layers. The second, more direct, approach involves a low temperature, low cost, and large-area-deposition method of chemical bath deposition (CBD) for the fabrication of CdS films to demonstrate the proof-of-principle integration of the novel spectrum splitting component into the prototype solar cell architectures.

CdS growth and properties: Structural, physical and electrical properties optimization of CBD CdS films were conducted first on borosilicate glass substrates. Using cadmium acetate as Cd and thiourea ($SC(NH_2)_2$) as sulfur precursor and ammonia as a complexing agent, CdS films were grown with varying sulfur concentration. Figure 9 is a typical θ-2θ X-ray diffraction (XRD) pattern of a CdS film on a borosilicate substrate showing the cubic nature of the film. Note that, irrespective of sulfur content, all films showed similar cubic peak reflections.

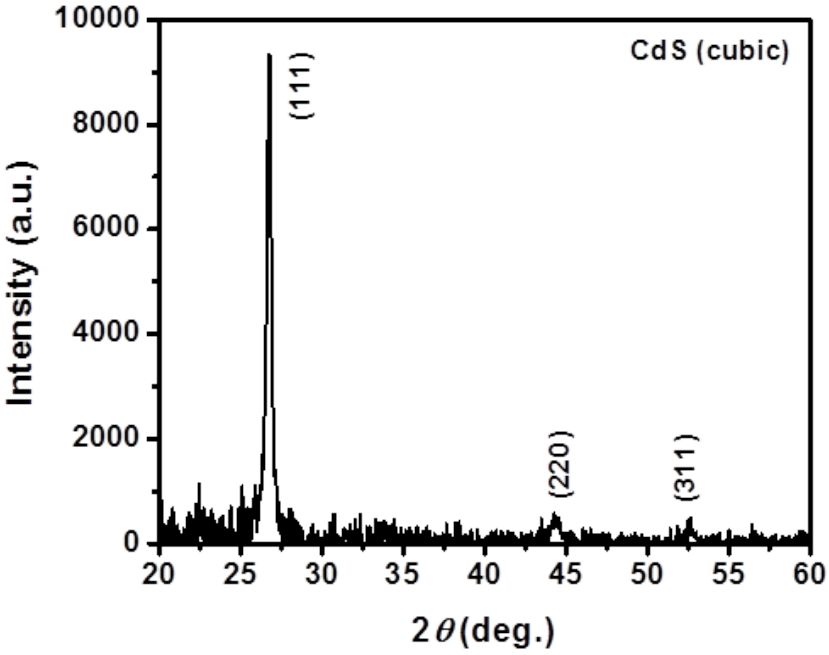

***Figure 12**: XRD pattern of a CdS films grown on a borosilicate glass template.*

The absorption measurement of the CdS thin films, measured at various wavelengths by a UV-visible spectrophotometer, was used to estimate the optical bandgaps (Fig. 13, center). Extrapolation of the linear portion of the curve to $\alpha^2 = 0$ gives the energy band gap of the films at different Cd:S concentrations. There is no systematic influence of sulfur content on the band gap energies has been observed (E_g values range from 2.3 to 2.4 eV). Accordingly, no appreciable difference is also noted from the morphological investigations. Regardless of sulfur content, all films displayed comparatively similar grain size and surface coverage, indicating the reproducibility of the CBD process.

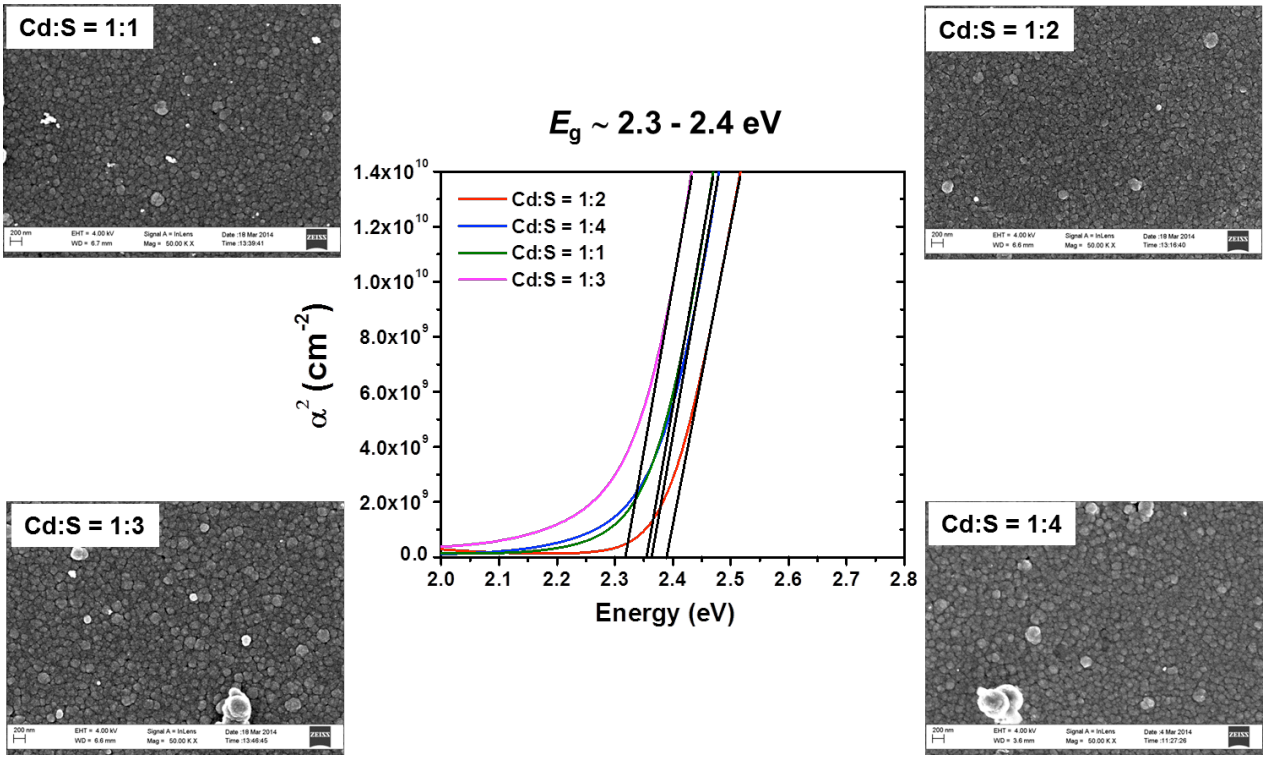

***Figure 13**: Optical band gap determination of CdS films with different Cd:S ratios (center plot, α^2 vs E). SEM images of the same samples presented in α^2 vs E plot are included for comparison.*

Fabrication of integrated sub-cells (by evaporation and inkjet printing).

The purpose of this task was to investigate the possibility of using vacuum-based evaporation to deposit one of the absorber layers and inkjet printing to deposit another. This allows us maximum flexibility to address any issues of inter-mixing of layers and also allows for the optimization of the absorber material parameters for best performance.

During this research, we have concentrated on process development through sputtering from single stoichiometric sources of CIS and CIGS materials, rather than the sequential deposition of single and binary elements of the absorber layers. Prior to absorber films, molybdenum layers with thicknesses in the range of 500-600 nm are deposited by *dc*-sputtering onto the soda-lime-glass substrates as the bottom electrode. The fabrication of CIS and/or CIGS layers were accomplished either as a single-cell or dual-cell geometry in an Ar environment at a substrate temperature of 400-550°C and a sputtering pressure of 5 mTorr. For the fabrication of subsequent CdS window and transparent electrode layers (i.e., ITO) chemical bath

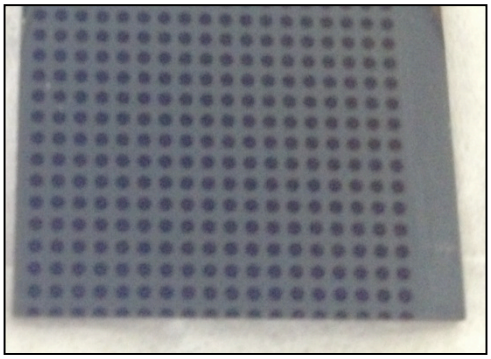

Fig 17. Photograph of a completed CIS/CdS/Mo/SLG sample. The circular high contrast regions are ITO electrodes.

deposition (CBD) and pulsed dc-sputtering were employed, respectively (Fig.17). Figure 18 demonstrates the I-V characteristics of a typical single junction solar cell. While the dark I−V curve clearly showed a strong rectifying behavior, the observed response did not significantly change under illumination, indicating that CIS/CIGS process needs to be further optimized to improve bulk/interface properties.

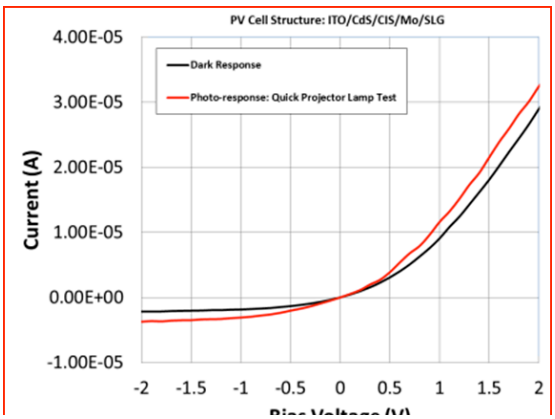

Fig. 18. Typical I−V characteristics in the dark(black) and under illumination (green) of a CIS/CdS/Mo/SLG sample.

To demonstrate the process flow for dual cell integration, both CIS and CIGS films have been fabricated on Mo-coated SLG substrates (Fig19, inset). Typical θ-2θ X-ray diffraction (XRD) patterns of the CIS and CIGS films are shown in Fig. 19. Other than Mo peaks arising from the bottom electrode both patterns displayed strong peak reflections indexed for CIS and CIGS phases. There is no evidence for secondary phase inclusions. Figure 20 shows the planar and cross-sectional morphologies of the CIS absorber. The precursor thin film presented has a dense film microstructure with small grains (~1 μm). Presumably, this can be originated either from the lower actual processing temperatures or loss of selenium during the sputter deposition or both. Clearly, further optimization of the processing conditions is needed to establish the necessary performance requirements for the absorber layers.

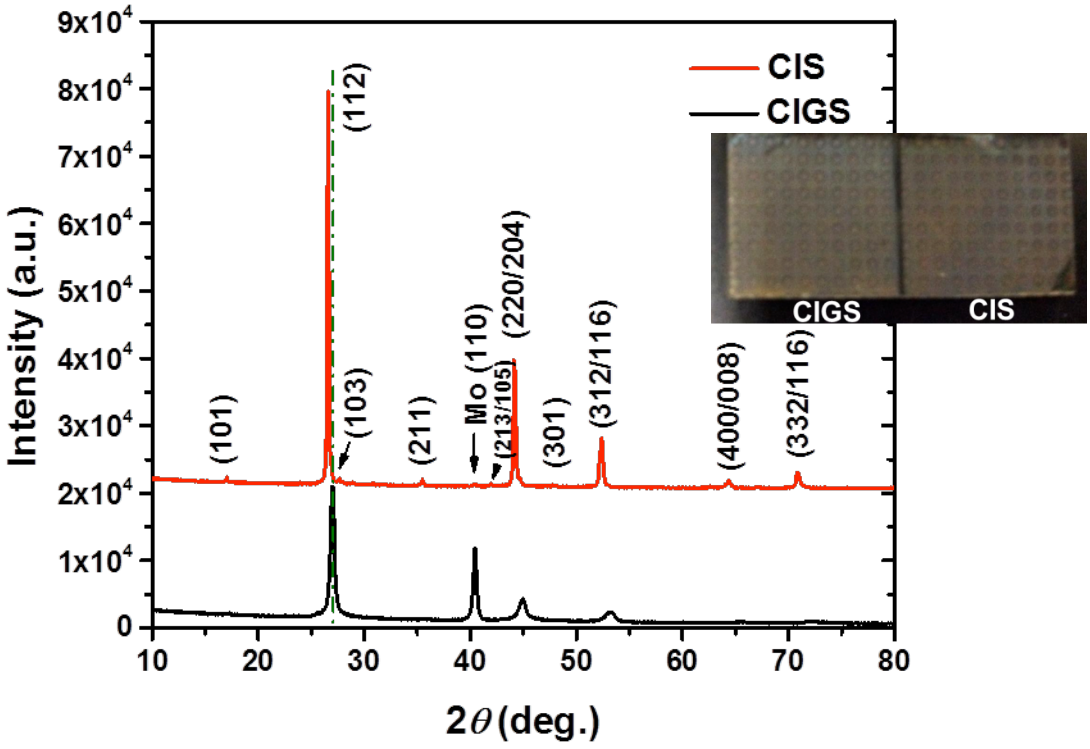

Fig. 19. The θ-2θ XRD scans of sputter deposited CIS (top pattern) and CIGS (bottom pattern) films on Mo/SLG substrates. Inset shows the photograph of the same sample after completed with CdS and ITO layers. Note that the two cells were separated from each other by using laser scribing.

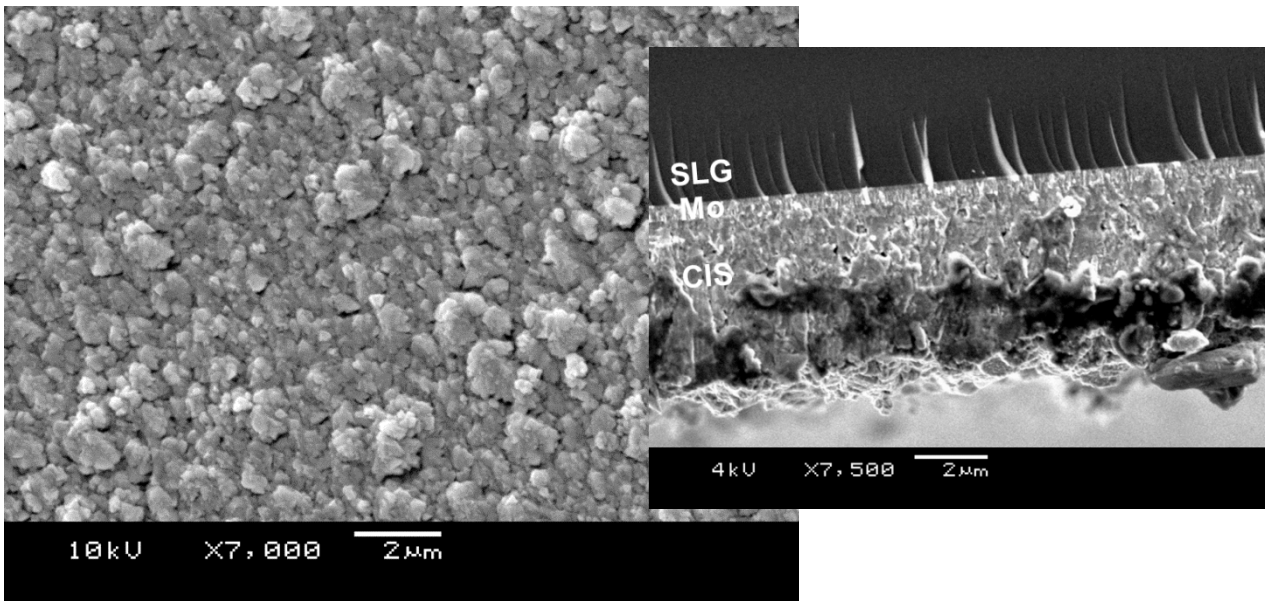

Fig. 20. Planar and cross-sectional SEM images of a sputter deposited CIS on Mo/SLG substrate.

Attempts were also made to further qualify the contact layer performance for PV applications using a partially processed CIGS test sample from Global Solar Energy, Inc. As shown in Fig. 21, a single junction solar cell was designed by depositing ITO and CdS contact layers on a partially processed CIGS cell from Global Solar Energy.

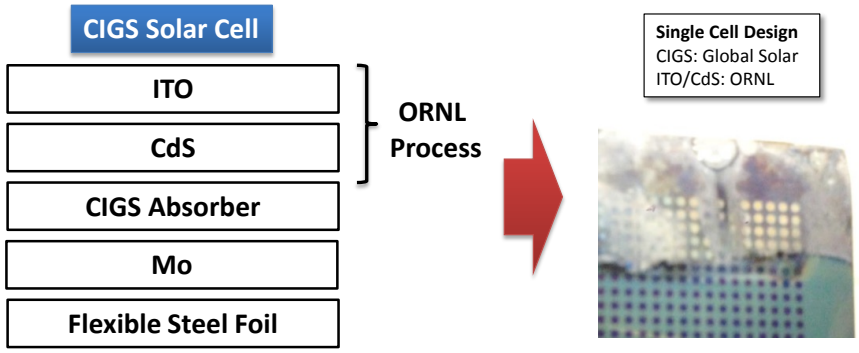

Fig. 21. Design of a single junction solar cell on a CIGS test sample from Global Solar Energy.

The single junction solar cell clearly established the impact of the window layers, as shown in Fig. 22, on the solar cell performance. The ITO layer directly deposited on the CIGS absorber layer resulted in a low open circuit voltage of about 0.26V. The V_{oc} value improved significantly to 0.60V for single junction solar cells with ITO/CdS stack deposited on the CIGS layer as expected due to better band alignment. The V_{oc} value of the cell processed at ORNL compared well with the open circuit voltage measured on a complete CIGS test cell obtained from Global Solar Energy. The observed results clearly indicate that the Mo, ITO, and CdS processes developed at ORNL are well-suited for CIGS cell development. The CIGS absorber layer processes need to be further improved for functional solar cell development.

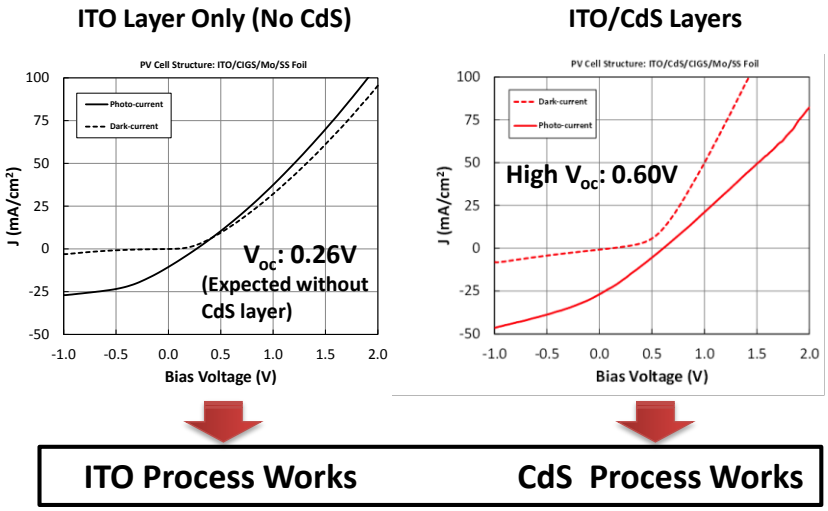

Fig. 21. Impact of the ITO and CdS layers on the open circuit voltage of single junction CIGS solar cells.

Unfortunately, the team at ORNL was unable to produce fully functional integrated solar cells for testing. The conclusion was that more time was needed to optimize the process. Therefore, we decided to pursue the prototypes with existing cells provided by NREL or commercially obtained.

Packaging & Characterization.

We packaged the device as described in detail in the last quarterly report. Here, we summarize the improvements we made in the final period for the characterization.
Wavelength Tests: The setup of the device (fig. 22) was such that the polychromat was placed in a distance of 163 mm to the CIGS-cell to get the best concentration of sunlight. Prior to the measurements an alignment process was required to align the gadget perpendicular to the sunlight. Therefore the device was adjusted manual, while the shadow of a little metallic rod (fig. 23) showed the aligning to the sun. When the structure is aligned right perpendicular, the shadow of the rod disappears.

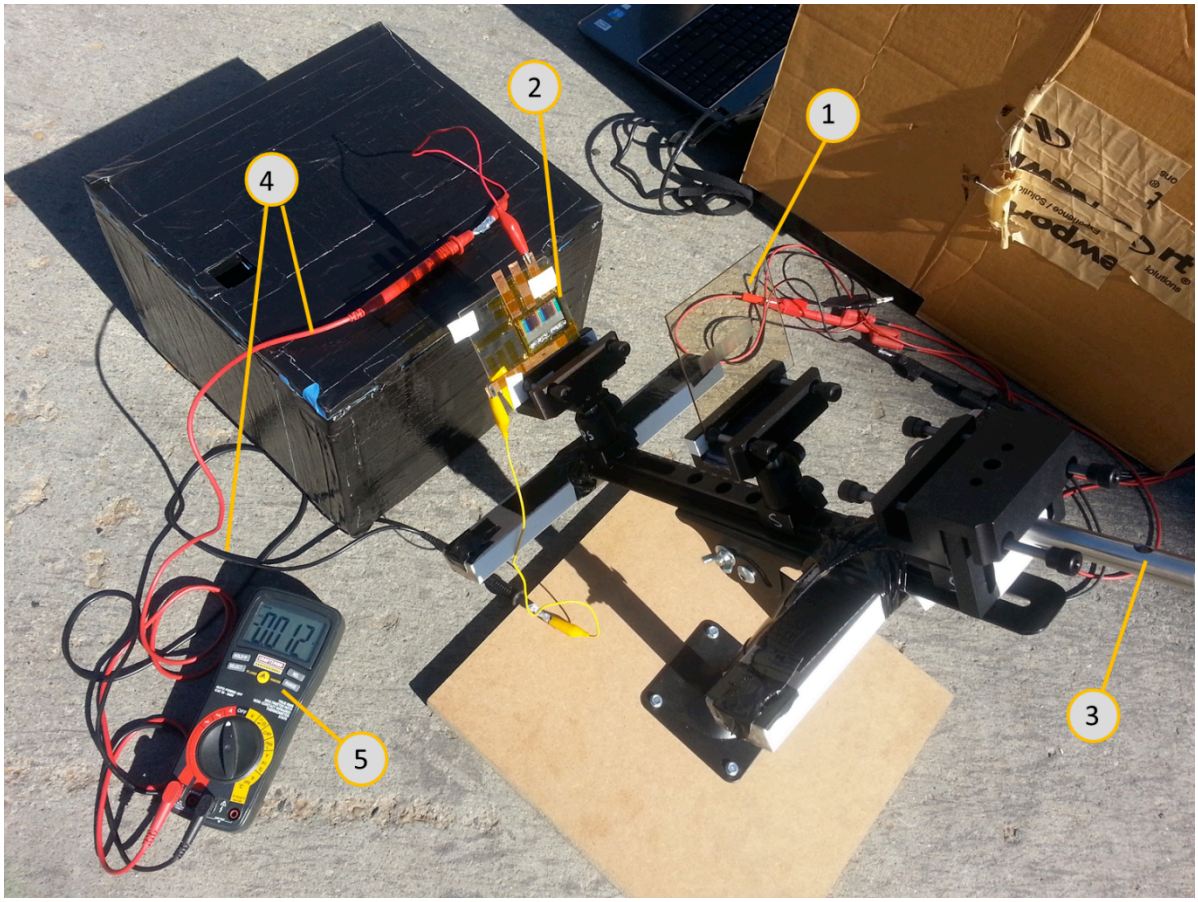

Fig. 22: Solar Concentrator setup with: 1 - Polychromat, 2 - CIGS-cell, 3 - aligning rod, 4 - connection wires, 5 - Multimeter


Fig. 23: Detailed illustration of the aligning rod with shadow

After the alignment the solar cells were connected with a Keithley 2602A measuring instrument which delivered a I-V-Curve. This procedure was done with and without polychromat for comparison. The most important parameter to compare – the maximum power density P_{Max} – was given by a MATLAB program.

$$P_{Max} = J_{SC} * V_{OC} * FF$$

J_{sc} is the short circuit current density at zero voltage, V_{oc} is the open circuit voltage at zero current and FF is the fill factor given by the solar cell which is a measure for the efficiency of the cell.

Comparing P_{Max} with and without polychromat gives the positive or negative power boost due to the diffractive optic by following equation:

$$\text{Power Boost} = (P_{Max\_Poly} - P_{Max\_Ref})/(P_{Max\_Ref}) * 100\ \%$$

In previous work the polychromat was fabricated so that there are three fields of light spectrum: a visable light zone, an infrared zone and an area where nearly no light arrives, the dark zone. Fig. 4 shows the light spectrum which is also periodically repeated because of the interference properties. First step in analyzing the polychromat was to figure out the power boost distribution of the CIGS-cell over the broadband spectrum of light. Distance between each measurement was 1 mm and an area of 8 mm width was analyzed. The results are shown in fig. 24.

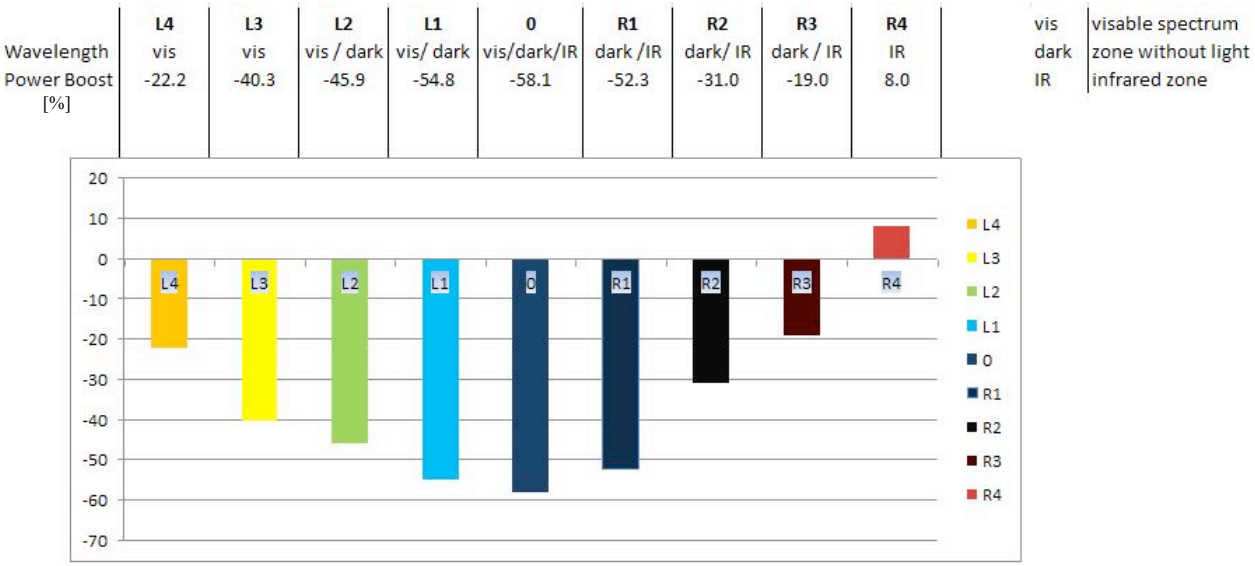

Fig. 24: Power Boost Distribution over the broadband spectrum of light.

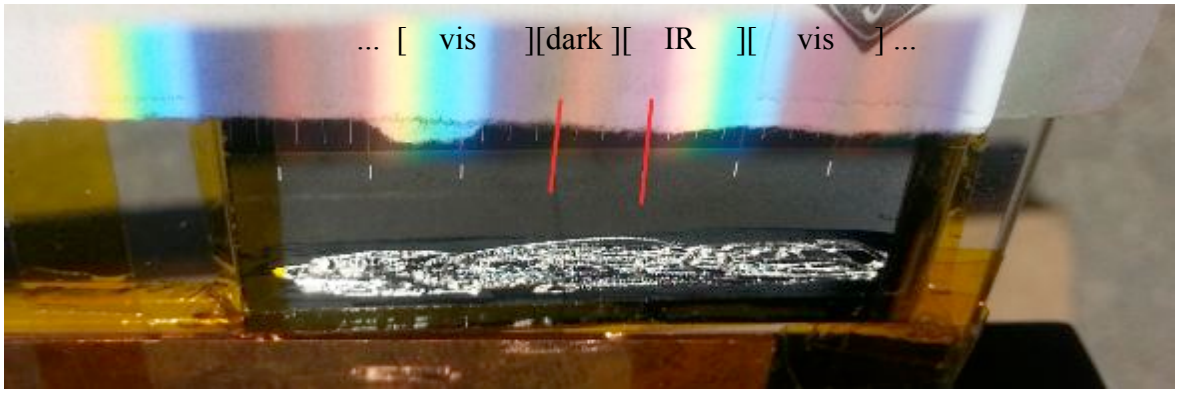

Fig. 25: Illustration of the spectrum splitted light with marking the measured solar cell with infrared area, which gave the only positive power boost named R4 in above fig. 24.

As can be seen in fig. 24, the infrared spectrum which is pictured in fig. 25 provides the highest power boost, what makes sense as the CIGS-cell works best in big wavelengths. To increase the power boost of 8% to at least 12% - which was the best result of previous measurements - a precise analysis of the infrared spectrum was necessary. Therefore a multimeter was used to find the point with the highest short circuit current, which was mentioned to be the point with the highest power boost as well. Starting from this position the area left and right was examined in steps of 0.33 mm to get an accurate overview of the systems tolerance.

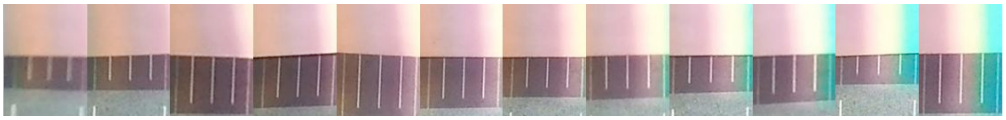

	L5	L4	L3	L2	L1	0	R1	R2	R3	R4	R5	R6
Position [mm]	-1.66	-1.33	-1	-0.66	-0.33	0	0.33	0.66	1	1.33	1.66	2
Boost 1 [%]	-3.9	0.1	6.4	9.3	11.0	13.2	11.9	9.6	6.8	3.2	-0.7	-3.6
Boost 2 [%]	-4.8	-0.6	1.9	8.4	10.7	12.9			6.5	2.6	-1.1	-4.3
Boost 3 [%]	-8.0	-1.6	-0.8	4.3	9.7	12.6	11.6	9.2	6.2	2.3	-1.9	-4.5
Aver. Boost [%]	**-5.6**	**-0.7**	**2.5**	**7.3**	**10.5**	**12.9**	**11.8**	**9.4**	**6.5**	**2.7**	**-1.2**	**-4.1**

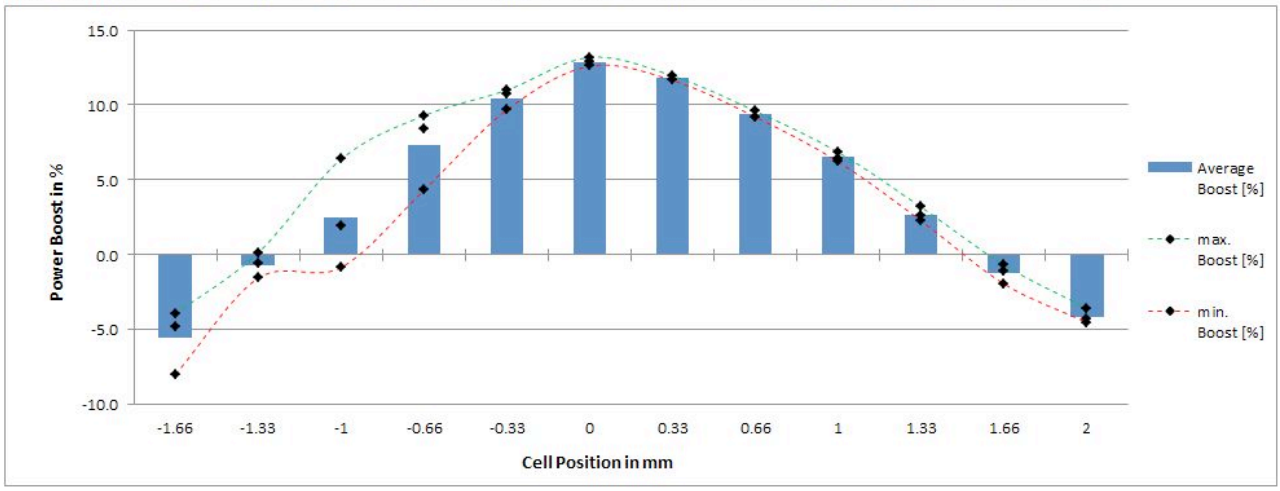

Fig. 26: Power boost distribution in the infrared area

Fig. 26 shows that the initial position, which was detected by the multimeter, actually provided the highest power boost. Right of this area (towards visible spectrum) the power boost fell slower than in the left area (towards infrared and dark spectrum). In each position 3 measurements were taken to show repeatability. By considering the green and the red curve in the diagraph it can be seen that the differences between measurements at one point in the left area are bigger than in right (visible light) area. Reason might be that the aligning to the sun is not perfectly the same in each measurement. Considering results of L4 and L5 it can be seen, that an aligning difference of only 0.33 mm decreases the power boost by almost 5%, so that in the dark zone even little changes in sun aligning have big influence on the results.

Error Analysis: To make an expressive evaluation of the functionality of the polychromat an comprehensive analysis of all parameters is necessary. Especially in outdoor experiments many factors can decrease the efficiency of the polychromat during the measuring process, so the task was to determine all those to prevent error sources.

Changing of sun position between measurements

There is time passing between two measurements so the sun changes its position and thus the light intensity varies. While short term experiments are less influenced by this factor, a long term experiment like the evaluation of the power boost over the whole band spectrum of light like in chapter 2 are more affected. Since the reference measurement (I-V-curve without polychromat) is taken at the beginning or end of the process, time difference to some compared measurements can be 15 – 20 min. In an experiment we determined the power boost difference from the polychromat and the reference by taking a measurement of the spectrum split by polychromat every minute for a quarter hour, than we took the reference curve. Before each measurement the structure was aligned to the sun again. The measurements started after the sun reached its highest point, which means that the light intensity was getting weaker.

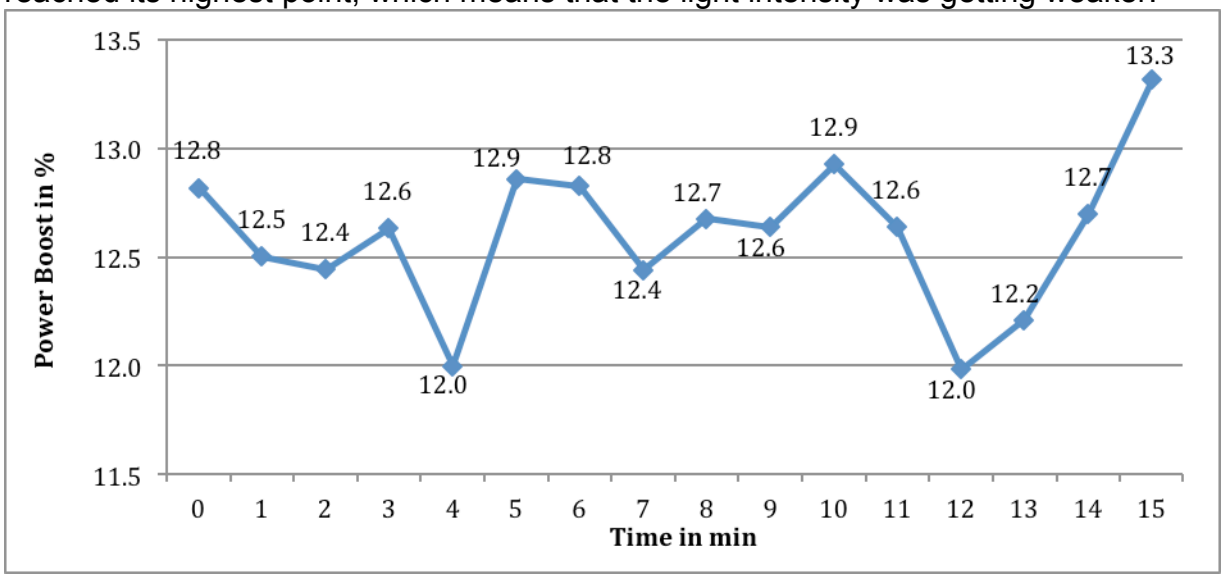

Fig. 27: Power Boost of the polychromat depending on the change of light intensity by time

As fig. 27 shows, there is no real dependence of the light intensity in a short time like 15 minutes. The average power boost is 12.6 % and a standard deviation of 0.3 % includes 12 of 16 measurements whereas the outliers might be result of measuring inaccuracies by the Keithley instrument.

Measuring inaccuracy

To figure out the accuracy of the measuring instrument (Keithley) a light with constant intensity and position was necessary. Therefore we did an indoor experiment illustrated in fig. 28. The light source was a flashlight that did not cover the AM 1.5 spectrum, but in our case it was just important to have a constant light source. First we aligned the solar cell and the polychromat perpendicular to the light and then we took 20 measurements in a very short time (time difference between each measurement approx. 30 sec.) without moving the position of the light or changing the power input for the lamp.

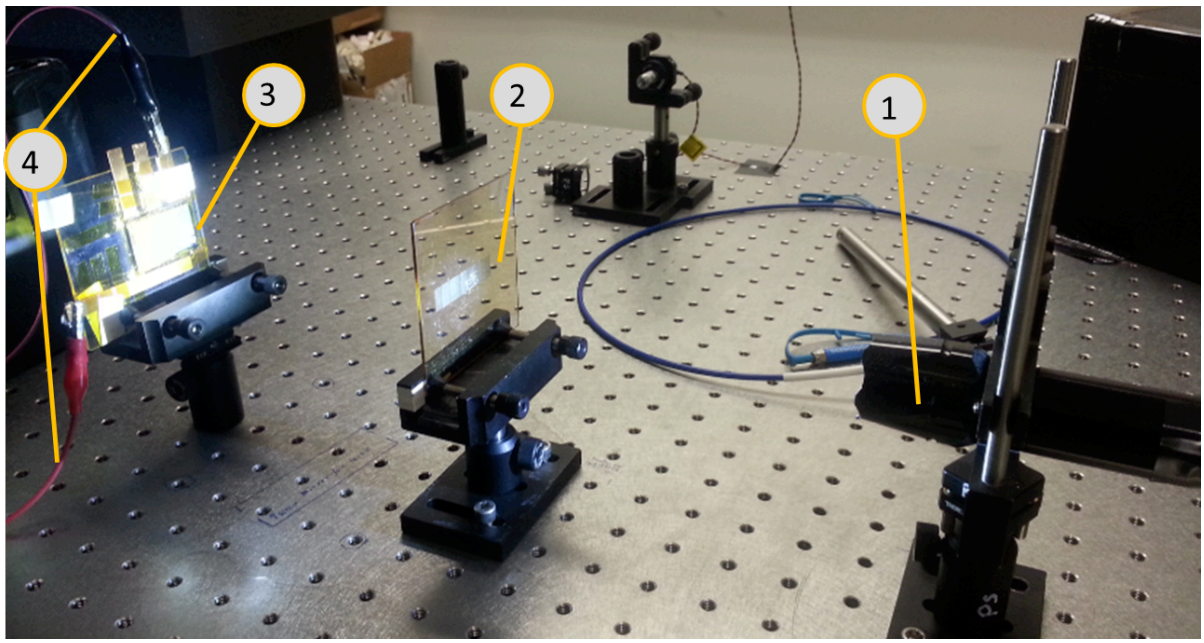

Fig. 28: Indoor Experiment setup with: 1 - light source, 2 - Polychromat, 3 - CIGS-cell, 4 - connection wires

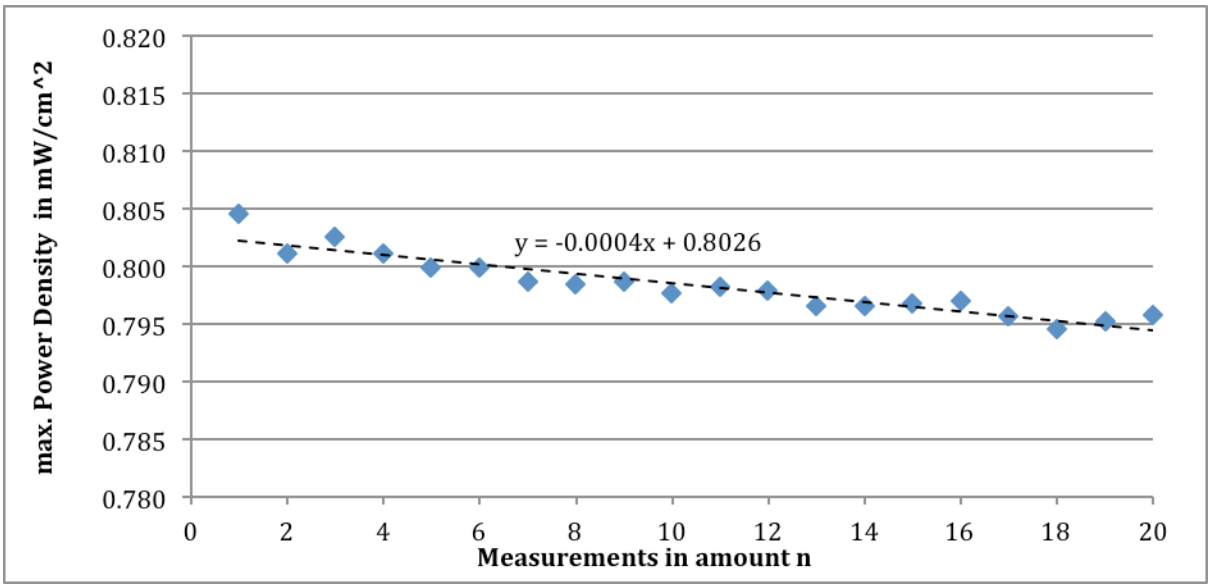

Fig. 29: Maximum power density of indoor polychromat measurements

In Fig. 29 it is shown that the results have a little down trend though it is very low with a slope of 4 x 10^{-4}. The lamp might have lost power very slightly since this down trend seems not to be a problem with the measuring instrument, because it has not appeared in previous experiments like in fig. 27. Moreover we can say that the Keithley instrument works very accurate since the standard deviation of the curve is only 2.5 x 10^{-3} mW/cm^2.

Black Box Test

Another parameter in the measuring process is the surrounding light that imping on the solar cells without passing through the polychromat. Therefore a box - called black box

(fig. 30) - was constructed to protect the solar cells from surrounding light. The sunlight could only pass in the box through a little window in the size of the polychromat aligned perpendicular to the sun. The result of the measurement was compared to measurements without box and without polychromat.

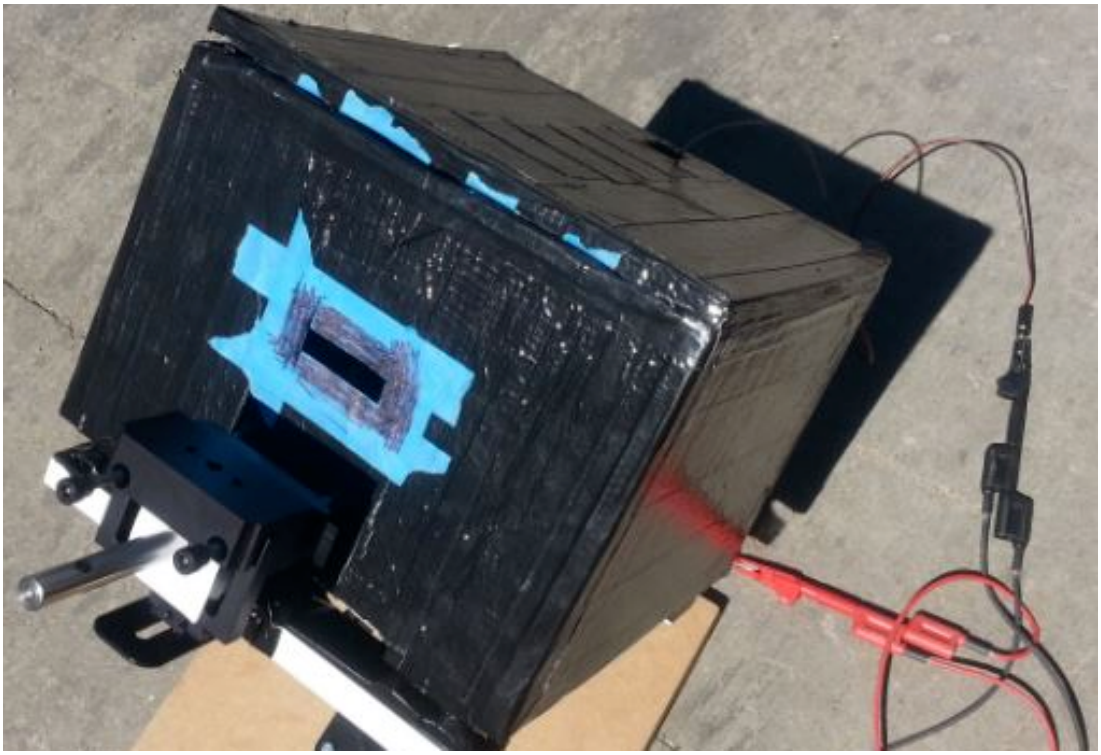

Fig. 30: Solar Concentrator setup covered by Black Box

Table 2: Power Boost of Polychromat with and without black box

Power Boost [%]	Polychromat	Polychromat + Black Box
Meas. 1	11.2	4.5
Meas. 2	11.1	3.0
Meas. 3	11.1	2.7
Average	**11.1**	**3.4**

The values in table 2 show that the black box decreases the efficiency of the polychromat. Even if surrounding light cannot impair the sun concentrator optic the power boost is lower. As a result of less incident light the intensity falls and the short circuit current is lower. This shows that surrounding light is positive for the solar concentrator even if disturbing wavelengths entering the cells in small amounts.

Periodicity of the polychromat

The concentrator optic is constructed such that the diffractive area is repeated periodically to increase the concentrator effect by interfering waves of the same wavelength. Grayscale lithography is used to insert a diffraction pattern into a glass optic. A laser is following a program code and works in nanometre scale. Height level errors in the pattern impair optimal diffraction [3]. As a result the interfering waves of the

periodically arranged patterns might not match anymore and disturbing wavelengths can interfere. In an experiment we tried to figure out, if the simple polychromat area is increasing the power boost compared to multiple diffractive areas. We covered the periodically repeating zones by a paper as can be seen in fig. 31. Then the Keithley instrument plotted the I-V-curve and subsequently the curves of the uncovered optic and the reference.

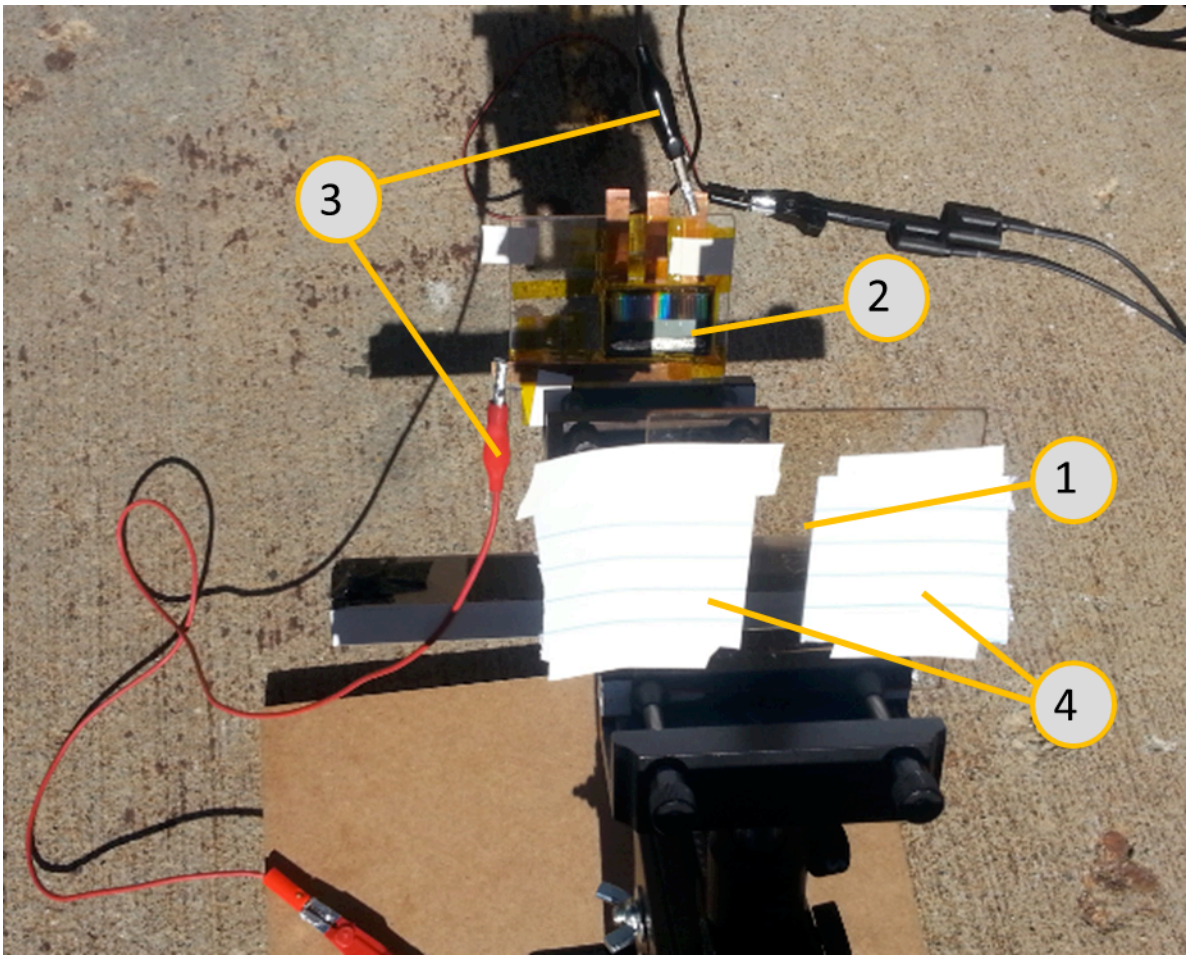

Fig. 31: Power boost measurement of non-periodically polychromat with: 1 - Polychromat, 2 - CIGS-cell, 3 - connection wires, 4 - optic covering papers

Table 3: Power Boost of Polychromat with and without periodically repeating pattern

Power Boost [%]	Polychromat period.	Polychromat non-period.
Meas. 1	9.7	-48.0
Meas. 2	9.6	-47.5
Meas. 3	10.1	-46.6
Average	**9.8**	**-47.4**

The results show that a non-periodically pattern dramatically drops in efficiency, so that it has a negative power boost compared to the single-junction cell without polychromat. As the periodically waves do not interfere anymore it is reasonable that efficiency drops. Also the light intensity is worse like in the black box.

Misalignment by time

Another effect on the polychromat efficiency is given by the misalignment of the cell due to the sun shift by time. Repeating of measurements to minimize statistical errors is important. Reminding on fig. 24 where the average boost of L3 was 4% different to the first measurement shows the necessity of multiple tests. Between those measurements only a few moments go by. As we know from earlier, the difference in light intensity due to sun shift in this time will not have big influence. In an experiment we now want to demonstrate the influence of the sun shift, when the apparatus is not aligned to the sun between each measurement. Therefore we repeated a measurement every minute for 5 minutes, without moving the device. In fig. 32 the moving of the interference pattern due to a sun shift in 5 minutes is illustrated. The change in efficiency of the polychromat is given in fig. 33 by the power boost.

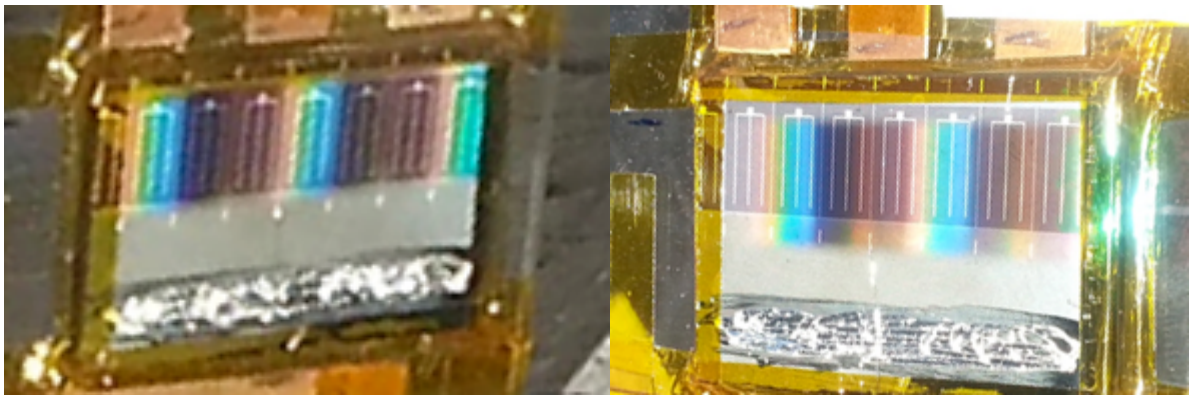

Fig. 32: Interference pattern at the beginning (a) and after 5 minutes (b)

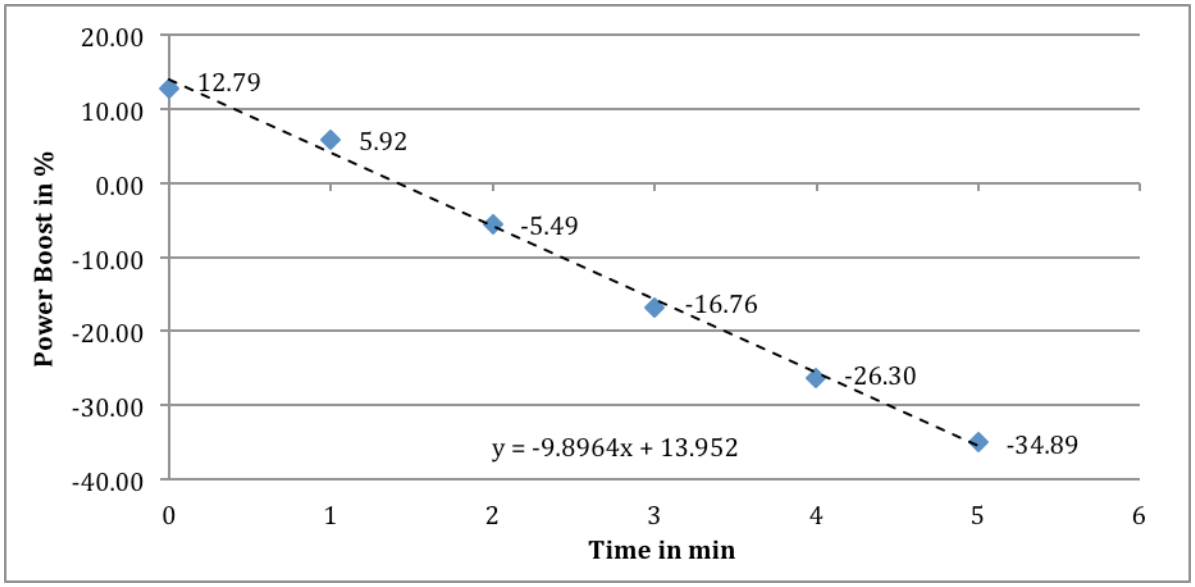

Fig. 33: Power boost development by time

Considering fig. 33 it can be said that a repeated measurement without aligning procedure causes a dramatically drop in the power boost by nearly 10 % every minute.

The importance of the alignment process even for short term experiments is illustrated by this diagram.

Conclusion

First, cell and polychromat has to be in the prescribed distance. Next they have to be aligned so that they are parallel and perpendicular to the sun. After all is aligned the position with the maximum power boost has to be determined. If this initial procedure is completed the solar concentrator can work efficiently. As the construction has to be aligned to the sun all the time, an automatic solar tracker would be needed for a costumer friendly design. For the laboratory experiments a manual alignment is sufficient, although long term experiments like daytime tests require a solar tracker, also the accuracy is higher. But even if all the error sources discussed earlier are heeded, the highest power boost of the solar concentrator has been 13.2 %. Compared with the simulation results in table 4 those results are more than 40 % lower.

Table 4: Simulation and measured results of important parameters

Parameters	Simulation	Measured
J_{SC} ref (mA/cm^2)	30.83	29.21
J_{SC} poly (mA/cm^2)	47.53	32.80
V_{OC} (V)	0.66	0.66
Fill Factor	0.776	0.770
P_{Max} ref (mW/cm^2)	15.79	14.71
P_{Max} poly (mW/cm^2)	24.34	16.65
Power Boost	54.14 %	13.18 %

Some further small errors are the heating of solar cells, dirty cells or diffractive optic surface or not perfectly aligned structure due to manual adjusting. However those errors will not cause the heavy loss of efficiency compared to the simulation results, since those factors impair both the polychromat and the reference measurement. Table 4 shows as well shows that only the polychromat offers big differences to the simulation. So the problem seems to be in the polychromat itself. One reason is the surfacing error, when scratches damage the diffracting area. This must be provided by carefully handling of the optic. The more important failure is caused by fabrication errors in the grayscale lithography. Even small divergences in height level of the structure can force misfits in the interference spectrum. Therefore the manufacturing of diffractive optics must be optimized and accelerated as the fabrication of the glasses take a long time and is not prepared for an industrialization process. But as the fabrication errors are known and could be provided in future the technology has the potential to grow to an important improvement of conventional single-junction cells, since power boost of 13.2% due to polychromats have already been proofed.

[1] R. Menon: “Increased photovoltaic power output via diffractive spectrum separation”, *PRL 110*, 123901, 2013

[2] R. Menon: “A new class of multi-bandgap high-efficiency photovoltaic enabled by broadband diffractive optics”, *Prog. Photovolt. Res. Appl.* 2015, 23, p. 1073 - 1079

[3] N. Mohammad: "Outdoor measurements of a photovoltaic system using diffractive spectrum-splitting and concentration*", AIP Advances 095311*, 2016, 6

Conclusions:

The key achievements during this project are:

1. We developed a rigorous and complete model for the design of the polychromat and most importantly significantly improved the computational efficiency.
2. We developed fabrication procedures for the polychromat. Perhaps, most importantly, we have identified several commercial vendors, who could manufacture the polychromat in the future.
3. We assembled a prototype system and characterized its performance both in ambient sunlight and under a solar simulator. This prototype was able to show an increase in efficiency of over 13%.
4. The ORNL team developed processes for inkjet printed solar cells as well as for evaporated solar cells. However, the integration of both processes was not completed.

Deliverables and Go/No Go Criteria from mid-review:

1. A polychromat of size ~1cm X 1cm in resist with spectrally-averaged optical efficiency of ~90%.

We have fabricated several polychromats of size 3cmX3cm. The highest spectrally averaged optical efficiency that we have so far is ~80% across the entire solar spectrum. At specific wavelengths, the efficiency has exceeded 90%. Some of the slightly lower efficiency is due to the inadequate knowledge of the dispersion data of the photoresist material. We have substantially met the goals of this milestone, and we will continue to improve the fabrication process and measurement of dispersion data in the next budget period in order to push these optical efficiencies even higher. Note that the more important metric is the increase in overall electrical power produced by the two cells under spectrum splitting. This broadly corresponds to high optical efficiency but at efficiencies of over 80%, the increase in power is marginal.

2. An integrated device of size ~0.5cm X 0.5cm containing two bandgaps with good current-voltage characteristics.

Bandgap tuned polymer solar cells have been developed and the process development for various CIGS thin film solar cell layers has been completed. The next step is the processing and characterization of discrete and integrated solar cells. This will be the intense effort for the next couple of months.

Final Milestones

1. Publications describing the process for fabricating the intergrated device, the prototype and its measurements.
    a. We completed several quarterly reports, this final report as well as many peer reviewed publications describing these.

2. Invention disclosures describing the process for fabricating the integrated device and incorporating the polychromat.
    a. Several invention disclosures were conducted for technologies that arose during this project, primarily for using the polychromat for spectroscopy.
3. Measurement data that shows conclusively that spectrum splitting with the polychromat allows for at least a 10% increase in power output from the integrated device (size ~ 0.5cm X 0.5cm) compared to a single bandgap control device under no spectrum split conditions.
    a. This was completed as described earlier.

The details from this project were disseminated via the peer-reviewed publications and conference presentations as listed below.

Full Author List	**Article Title**	**Journal Name**
G. Kim, J-A. Dominguez-Caballero, H. Lee, D. Friedman and R. Menon	Increased photovoltaic power output via diffractive spectrum separation	Physical Review Letters
P. Wang and R. Menon	Optimization of generalized dielectric nanostructures for enhanced light trapping in thin-film photovoltaics via boosting the local density of optical states	Optics Express
R. Menon	Enhancing the efficiency of photovoltaics with photonics	SPIE Newsroom
B. Shen, P. Wang and R. Menon	Optimization and analysis of 3D nanostructures for power-density enhancement in ultra-thin photovoltaics under oblique illumination	Optics Express
P. Wang, J-A. Dominguez-Caballero, D. Friedman and R. Menon	A new class of multi-bandgap high efficiency photovoltaics enabled by broadband diffractive optics	Progress in Photovoltaics: Research & Applications
P. Wang and R. Menon	Computational spectroscopy based on a broadband diffractive optic	Optics Express
P. Wang and R. Menon	Computational spectroscopy via singular-value decomposition and regularization	Optics Express
N. Mohammad, P. Wang, D. J. Friedman and R. Menon	Enhancing photovoltaic output power by 3-band spectrum-splitting & concentration using a diffractive micro-optic	Optics Express
T. Aytug, et al.	Monolithic graded-refractive-index glass-based antireflective coatings: Broadband omnidirectional light harvesting and self-cleaning characteristics	J. Mater. Chem. C
N. Mohammad, M. Schulz, P. Wang, and R. Menon	Outdoor measurements of a photovoltaic system using diffractive spectrum-splitting & concentration	AIP Advances

Full Author List	Paper Title	Presented in the Season/Symposium Name at Conference Name	Conference Location	Dates
R. Menon	Nanophotonics for light-management in thin-film photovoltaics and optical nanopatterning for their fabrication	SPIE Photonics West	San Francisco	Feb-14
P. Wang, B. Shen and R.	Optimization of generalized nanostructures for light trapping beyond the ergodic limit	OSA Topical meeting on Nanostructures and advanced materials for photovoltaics	Tucson	Nov 3-6, 2013
P. Wang, B. Shen and R.	Optimization of nanostructures for enhanced light-trapping in thin-film photovoltaics	OSA Frontiers in Optics	Orlando	Oct. 6-10, 201
P. Wang, J A. Dominguez-Caballero, D. J. Friedman and R. Menon	Multi-bandgap high- efficiency photovoltaics enabled by broadband diffractive optics	OSA Topical meeting on Optics for Solar Energy	Tucson	Nov 3-6, 2014
R. Menon	Digital metamaterials & micro-optics for photonics and imaging	Tech Talk at 3M	Minneapolis, MN	3/11/15
N. Mohammad, P. Wang, D. J. Friedman, K. Ramanathan, L. Mansfield and R. Menon	Microphotonic spectrum-splitting and concentration for high-efficiency photovoltaics	CLEO	San Jose, CA	5/12/15
R. Menon	Digital metamaterials & micro-optics for photonics & imaging	EIPBN	San Diego, CA	5/28/15
P. Wang and R. Menon	Computational color imaging with enhanced light sensitivity based on a microstructured diffractive element array	OSA IS	Arlington, VA	6/10/15
P. Wang, N. Mohammad, M. Schulz and R. Menon	Ultra-high efficiency photovoltaics via diffractive optics	OSA PV Topical Meeting	Suzhou China	Nov. 3, 2016
R. Menon	Digital metamaterials and micro-optics for photonics and imaging	International Microphotonics Congress Expo	Berlin, Germany	Oct. 11, 2016

Budget and Schedule:

The budget for this Project was $449,814, and the Project was spent prior to the close of the performance period. The total variances that we had between budget categories is approximately 8.26%, which is well within the realm of what is allowable under 25%. There was no change in budget period schedules except for a 1-year no-cost extension that was requested for the last period. The start date was October 1, 2012 and end date was August 14, 2016.

Path Forward:

There are 3 thrusts of future development that we would like to pursue.

The first is to improve the computational scalability of the design software even more by use the massively parallel GPU architectures or via commercial cloud computing capabilities (like the Google cloud). This would be required if one were to scale up the design of the polychromat to much larger sizes.

The second is to work closely with commercial vendors for the manufacture of the polychromat. We have already identified several companies, who could perform this task with potential for low cost at large volumes. This will also ensure the repeatability and accuracy of the polychromat, problems that we faced in the University labs.

The third is to work closely with materials scientists at NREL to optimize absorber materials that are well suited for the polychromat architecture. We have already begun an informal collaboration with a few groups to explore this thrust. Eventually, this would have to be followed up with commercial partners to bring this technology to the market.

The following patent application arose out of the work conducted under this research.

R. Menon, “System and method for extraction of spectral information from a limited data set,” technology disclosure submitted March 7, 2013.

References:

Please see the references included in the respective sections above.